

Minkowski tensors for voxelized data: robust, asymptotically unbiased estimators

D. Hug^{*}, M.A. Klatt[†] and D. Pabst^{*}

Abstract

Minkowski tensors, also known as tensor valuations, provide robust n -point information for a wide range of random spatial structures. Local estimators for voxelized data, however, are unavoidably biased even in the limit of infinitely high resolution. Here, we substantially improve a recently proposed, asymptotically unbiased algorithm to estimate Minkowski tensors for voxelized data. Our improved algorithm is more robust and efficient. Moreover we generalize the theoretical foundations for an asymptotically bias-free estimation of the interfacial tensors to the case of finite unions of compact sets with positive reach, which is relevant for many applications like rough surfaces or composite materials. As a realistic test case, we consider, among others, random (beta) polytopes. We first derive explicit expressions of the expected Minkowski tensors, which we then compare to our simulation results. We obtain precise estimates with relative errors of a few percent for practically relevant resolutions. Finally, we apply our methods to real data of metallic grains and nanorough surfaces, and we provide an open-source python package, which works in any dimension.

Keywords: tensor valuations, microstructure characterization, anisotropy, digitized image analysis

2020 MSC: 94A08 · 68U10 · 60D05 · 53C65 · 28A75 · 62H35 · 52A22

^{*}Karlsruhe Institute of Technology, Institute for Stochastics, 76131 Karlsruhe, Germany

[†]German Aerospace Center (DLR), Institute for AI Safety and Security, Wilhelm-Runge-Str. 10, 89081 Ulm, Germany; German Aerospace Center (DLR), Institute for Material Physics in Space, 51170 Köln, Germany; Department of Physics, Ludwig-Maximilians-Universität München, Schellingstr. 4, 80799 Munich, Germany

Contents

1	Introduction	2
2	Minkowski tensors in integral geometry	3
3	Asymptotics for estimators: a theoretical foundation	7
4	Algorithms to estimate Minkowski tensors	10
4.1	Description and analysis	11
4.2	Implementation	21
4.3	Choice of parameters	21
4.4	Convex test cases	22
4.5	Nonconvex test cases	23
5	Isotropic random polytopes	25
5.1	Exact expectations	25
5.2	Simulation study	27
6	Experimental data	28
6.1	Metallic grains	28
6.2	Nanorough surfaces	30
A	Further simulation results	37

1 Introduction

Random spatial structures appear ubiquitously in nature and technology. Examples (and their corresponding mathematical models) are heterogeneous materials and porous media (random sets) [44, 64, 45, 1, 3], cellular tissues and foam-like structures (tessellations) [46, 50, 34, 60], rough surfaces (random fields) [2, 65, 59, 51], and bacterial colonies (particle processes) [12, 19, 66] as well as error-correcting code (high-dimensional sphere packings) [67, 13]. This variety of examples corresponds to a similar diversity in random shapes.

In all of these cases, Minkowski tensors (also known as tensor valuations) [55, 28] provide a comprehensive, unified shape analysis. The Minkowski tensors [57] are generalizations of the well-known Minkowski functionals (or intrinsic volumes) from integral geometry [55]; see Section 2 for more details and the theoretical background. The intrinsic volumes represent intuitive geometric information, e.g., on the volume, surface area, or curvature; the Minkowski tensors additionally distinguish different orientations with respect to these geometrical properties [37].

Minkowski tensors of different ranks capture symmetries of all orders. They quantify the degree of anisotropy as well as the preferred directions. They are comprehensive in the sense of Hadwiger’s and Alesker’s characterization theorems [55], intuitively speaking, they contain all motion-covariant, continuous, and additive shape information. Since they are additive, Minkowski functionals and tensors provide robust access to n -point information [41]. Moreover, the definition in real space allows for a convenient treatment of boundary conditions [56].

The versatility of Minkowski functionals and tensors is demonstrated by their ample successful applications in a wide range of fields, including statistical physics [40, 42, 33], biology [8, 7, 6], spatial statistics [66, 16], image analysis [44, 45], as well as astronomy and cosmology [18, 52, 30, 35, 15, 14]. Explicit examples of random spatial structures characterized via Minkowski functionals and tensors are porous media [5, 4, 36, 3, 29], composite materials [17], nanorough surfaces [59], fluid demixing [10], and trabecular bone [50, 37, 11].

A challenge, however, is the application of Minkowski tensors to voxelized data because the discrete set of available orientations introduces a systematic bias usually even in the limit of infinitely high resolution. For gray-scale data, marching-cube algorithms can turn the voxelized data into triangulated meshes with continuous orientations, which results in asymptotically bias-free algorithms [39, 38, 61, 62]. If no gray-scale data is available, any local algorithm on black-and-white voxels will be asymptotically biased, i.e., the estimator will not converge to the true value in the limit of infinite resolution [63].

An algorithmic solution to the problem was recently proposed in [21], which had been inspired by [43]. The key idea is to construct Voronoi cells that can encode global information and thus guarantee asymptotically bias-free estimators of all Minkowski tensors for sets of positive reach. This requirement of a positive reach, however, excludes many interesting applications, like rough surfaces and composite materials. More importantly, the proposed algorithm suffered from numerical instabilities since it relies on a matrix inversion.

Here, we substantially advance the robustness of the algorithm by replacing the matrix inversion by a least squares fit. We, moreover, increase its efficiency by using an unbiased estimator of the Voronoi volume integrals. This revised algorithm is also asymptotically unbiased for sets of positive reach, as we prove rigorously. We demonstrate its robustness and accuracy for exemplary cases of geometric shapes, stochastic models, and real data.

Even for a simple example of a set without positive reach, our algorithm achieves surprisingly good results (with relative deviations of less than 3% in the eigenvalues of the interfacial tensors, see Table 6). Since such precision is not theoretically substantiated, we also introduce an alternative method to estimate interfacial tensors, for which we are able to prove that it is asymptotically unbiased even for finite unions of compact sets with positive reach.

Together with the paper, we publish an open-source python package including both methods. It is the first implementation of Minkowski tensors that we know of that can be applied to any dimension. It can also be applied to any discrete representation of the set, i.e., not only for pixelated images, but representations using non-cubic lattice or even random point patterns. The last generalization is especially helpful in high dimensions, where similar to numerical integration, lattice representations may converge too slowly. Details on the algorithm, implementation, and suitable choices of parameters are discussed in Sections 4.1–4.3.

We demonstrate the reliability of our methods for simple geometric test cases in Sections 4.4 and 4.5. For a stochastic test case, we apply our estimator to a classic example of random convex sets, isotropic random polytopes (see Section 5), both in theory (see Section 5.1) and simulations (see Section 5.2).

In Section 6, we turn to experimental data. First, we analyze metallic grains in a polycrystalline nickel-based superalloy using data from [60]. The Minkowski tensors characterize the cells to be distinctly more anisotropic with respect to curvature than the surface area (see Section 6.1). Then, we determine the interfacial tensors of nanorough surfaces from [59] (see Section 6.2).

2 Minkowski tensors in integral geometry

In this section, we provide a brief introduction to Minkowski tensors (or tensor valuations) and summarize their basic properties. Let \mathcal{K}^d denote the set of all compact convex subsets

(convex bodies) of \mathbb{R}^d . We denote by $\langle \cdot, \cdot \rangle$ and $\|\cdot\|$ a Euclidean scalar product and the induced norm. We write $B^d := \{x \in \mathbb{R}^d : \|x\| \leq 1\}$ for the Euclidean unit ball centered at the origin o and $\mathbb{S}^{d-1} = \partial B^d = \{x \in \mathbb{R}^d : \|x\| = 1\}$ for its boundary. The volume of B^d is denoted by $\kappa_d = \pi^{d/2}/\Gamma(1 + d/2)$ and $\omega_d = d\kappa_d$ is its surface area, i.e., the $(d - 1)$ -dimensional volume of \mathbb{S}^{d-1} . The intrinsic volumes $V_i : \mathcal{K}^d \rightarrow [0, \infty)$, $i \in \{0, \dots, d\}$, are a collection of $d + 1$ basic functionals on \mathcal{K}^d that are distinguished by their properties:

- They form a basis of the vector space of continuous, isometry invariant, additive, functions on \mathcal{K}^d ; V_i is positively homogeneous of degree i [26, Theorem 4.20].
- They arise as coefficient functionals of a Steiner formula [26, Theorem 3.10].
- They satisfy various integral geometric formulas such as Crofton formulas, projection formulas and (intersectional as well as additive) kinematic formulas [26, Chap. 5].
- They can be additively extended to polyconvex sets (finite unions of compact, convex sets) and play a key role in the classical theory of geometric valuations (see [54, Chap. 1] and [26, Chap. 4.5]).

The intrinsic volumes have also been called Minkowski functionals (or quermassintegrals, though with a different normalization and notation). Due to their properties, the Minkowski functionals are useful descriptors that can be applied for the analysis of complex spatial structure.

Since the Minkowski functionals are isometry invariant, their usefulness in characterizing anisotropic features of objects under investigation is limited. The Minkowski tensors (see [25, Chap. 2]), which we introduce next, provide a more general set of tensor-valued geometric descriptors that are sensitive to position and orientation of geometric objects in Euclidean space. We start by providing a brief introduction to symmetric tensors and tensor-valued functionals as needed for the present purpose.

In the following, we use the scalar product of \mathbb{R}^d to identify \mathbb{R}^d with its dual space, hence a vector $a \in \mathbb{R}^d$ will be identified with the linear functional $x \mapsto \langle a, x \rangle$ from \mathbb{R}^d to \mathbb{R} . For $r \in \mathbb{N}_0$, an r -tensor, or tensor of rank r , on \mathbb{R}^d is an r -linear mapping from $(\mathbb{R}^d)^r$ to \mathbb{R} . The vector space of all r -tensors of \mathbb{R}^d has dimension d^r . If e_1, \dots, e_d is the standard basis of \mathbb{R}^d , then the r -tensors $e_{i_1} \otimes \dots \otimes e_{i_r}$, $1 \leq i_1, \dots, i_r \leq d$, are a basis of the vector space of all tensors of rank r in \mathbb{R}^d . Here we have $e_{i_1} \otimes \dots \otimes e_{i_r}(x_1, \dots, x_r) = \prod_{j=1}^r \langle e_{i_j}, x_j \rangle$ for $x_1, \dots, x_r \in \mathbb{R}^d$.

A tensor is *symmetric* if it is invariant under permutations of its arguments. By $\mathbb{T}^r(\mathbb{R}^d)$, or simply by \mathbb{T}^r , we denote the real vector space (with its standard topology) of symmetric r -tensors on \mathbb{R}^d . We define $\mathbb{T}^0 = \mathbb{R}$, and, by the identification made above, we have $\mathbb{T}^1 = \mathbb{R}^d$. In any case, $\dim \mathbb{T}^r(\mathbb{R}^d) = \binom{d+r-1}{r}$.

The *symmetric tensor product* $a_1 \odot \dots \odot a_k \in \mathbb{T}^{r_1 + \dots + r_k}$ of $a_i \in \mathbb{T}^{r_i}$, $i = 1, \dots, k$, is a symmetric tensor of rank $r_1 + \dots + r_k$. Denoting by $\mathcal{S}(m)$ the group of bijections of $\{1, \dots, m\}$, $s_0 := 0$ and $s_i := r_1 + \dots + r_i$, for $i = 1, \dots, k$, it is defined by

$$(a_1 \odot \dots \odot a_k)(x_1, \dots, x_{s_k}) := \frac{1}{s_k!} \sum_{\sigma \in \mathcal{S}(s_k)} \prod_{i=1}^k a_i(x_{\sigma(s_{i-1}+1)}, \dots, x_{\sigma(s_i)})$$

for $x_1, \dots, x_{s_k} \in \mathbb{R}^d$. In this way, the space of symmetric tensors (of arbitrary rank) becomes an associative, commutative algebra with unit. For symmetric tensors a, b, a_i we will use the

abbreviations $a \odot b =: ab$ and $a_1 \odot \cdots \odot a_k =: a_1 \cdots a_k$, and we write a^r for the r -fold symmetric tensor product of a , if $r \in \mathbb{N}$, and $a^0 := 1$. If $r_1 = \dots = r_k = 1$ and $x_1, \dots, x_k \in \mathbb{R}^d$, then

$$a_1 \cdots a_k(x_1, \dots, x_k) = \frac{1}{k!} \sum_{\sigma \in \mathcal{S}(k)} \prod_{i=1}^k \langle a_i, x_{\sigma(i)} \rangle,$$

and hence, for $a \in \mathbb{R}^d$ and $r \geq 1$, the r -fold symmetric tensor product of a satisfies

$$a^r(x_1, \dots, x_r) = \langle a, x_1 \rangle \cdots \langle a, x_r \rangle.$$

The scalar product, $Q(x, y) = \langle x, y \rangle$, $x, y \in \mathbb{R}^d$, is a symmetric tensor of rank two; we call Q the *metric tensor*. Clearly, if e_1, \dots, e_d is an orthonormal basis of \mathbb{R}^d , then $Q = e_1^2 + \cdots + e_d^2$.

Let (e_1, \dots, e_d) be an orthonormal basis of \mathbb{R}^d . Then the symmetric tensors $e_{i_1} \cdots e_{i_r}$ with $1 \leq i_1 \leq \cdots \leq i_r \leq d$ form a basis of $\mathbb{T}^r(\mathbb{R}^d)$. The corresponding coordinate representation of $T \in \mathbb{T}^r(\mathbb{R}^d)$ is

$$T = \sum_{1 \leq i_1 \leq \cdots \leq i_r \leq d} t_{i_1 \dots i_r} e_{i_1} \cdots e_{i_r} \quad \text{with} \quad t_{i_1 \dots i_r} = \binom{r}{m_1 \dots m_d} T(e_{i_1}, \dots, e_{i_r}), \quad (2.1)$$

where $m_k := |\{\ell \in [r] : i_\ell = k\}| \in \{0, \dots, r\}$, $k = 1, \dots, d$, counts how often the number k appears among the indices i_1, \dots, i_r . In particular, for $d = r = 2$, we have $T(e_1, e_1) = t_{11}$, $T(e_2, e_2) = t_{22}$ and $T(e_1, e_2) = T(e_2, e_1) = \frac{1}{2}t_{12}$, hence $T = T(e_1, e_1)e_1^2 + 2T(e_1, e_2)e_1e_2 + T(e_2, e_2)e_2^2$ with $2T(e_1, e_2)e_1e_2 = T(e_1, e_2)e_1e_2 + T(e_2, e_1)e_2e_1$.

For $T \in \mathbb{T}^r(\mathbb{R}^d)$ we introduce a norm by

$$|T| := \sup\{|T(x_1, \dots, x_r)| : x_i \in \mathbb{R}^d, \|x_i\| \leq 1, i = 1, \dots, r\}.$$

If $a_i \in \mathbb{T}^{r_i}$, $i = 1, \dots, k$, then

$$|a_1 \odot \cdots \odot a_k| \leq |a_1| \cdots |a_k|. \quad (2.2)$$

In particular, if $x \in \mathbb{R}^d$ and $u \in \mathbb{S}^{d-1}$, then $|x^r u^s| \leq \|x\|^r$. Moreover, if $x_1, \dots, x_m \in \mathbb{R}^d$ and $y_1, \dots, y_m \in \mathbb{R}^d$, then

$$\left| \bigodot_{i=1}^m x_i - \bigodot_{i=1}^m y_i \right| \leq \sum_{j=1}^m \|x_j - y_j\| \prod_{i=1}^{j-1} \|x_i\| \prod_{i=j+1}^m \|y_i\|. \quad (2.3)$$

For $T \in \mathbb{T}^r(\mathbb{R}^d)$ and a rotation $\vartheta \in O(d)$ of \mathbb{R}^d , we define the operation of ϑ on T in such a way that the resulting tensor $\vartheta T \in \mathbb{T}^r(\mathbb{R}^d)$ is given by $(\vartheta T)(x_1, \dots, x_r) = T(\vartheta^{-1}x_1, \dots, \vartheta^{-1}x_r)$ for $x_1, \dots, x_r \in \mathbb{R}^d$.

In order to introduce the basic Minkowski tensors of (nonempty) convex bodies, we use the support measures which can be considered as local versions of the intrinsic volumes. For a convex body $K \subset \mathbb{R}^d$, the support measure $\Lambda_j(K, \cdot)$ is a Borel measure on $\mathbb{R}^d \times \mathbb{S}^{d-1}$ which satisfies a local Steiner formula and $\Lambda_j(K, \mathbb{R}^d \times \mathbb{S}^{d-1}) = V_j(K)$ for $j \in \{0, \dots, d-1\}$. For basic properties of the support measures and a representation in the case where K is a polytope, we refer to [53, Chapter 4.2]. The maps $K \mapsto \Lambda_j(K, \cdot)$ are measure-valued, additive (valuations), weakly continuous and for Borel sets $\alpha \subseteq \mathbb{R}^d$ and $\beta \subseteq \mathbb{S}^{d-1}$ they satisfy the covariance condition $\Lambda_j(gK, g\alpha \times g_0\beta) = \Lambda_j(K, \alpha \times \beta)$, where $g : \mathbb{R}^d \rightarrow \mathbb{R}^d$ is a rigid motion and g_0 is its rotational part (that is, $g(x) = g_0(x) + t$ for $x \in \mathbb{R}^d$, where $t \in \mathbb{R}^d$ is a translation vector and g_0 is a

rotation). More generally, the support measures have been defined (as signed measures) for the more general class of sets of positive reach (see [49, Chapter 4] for an introduction) and for finite unions of compact sets with positive reach all of whose finite intersections have again positive reach (see [49, Chapter 5] and the literature cited there); the corresponding class of sets in \mathbb{R}^d is denoted by \mathcal{U}^d . In fact, extensions of these measures to arbitrary closed subsets of \mathbb{R}^d have been studied in [23, 24] and will be considered in Section 3.

If K is a convex body or a compact set with positive reach, then the basic *Minkowski tensors* of K are defined by

$$\Phi_k^{r,s}(K) := \frac{1}{r!s!} \frac{\omega_{d-k}}{\omega_{d-k+s}} \int_{\mathbb{R}^d \times \mathbb{S}^{d-1}} x^r u^s \Lambda_k(K, d(x, u)) \quad (2.4)$$

for $k = 0, \dots, d-1$ and $r, s \in \mathbb{N}_0$,

$$\Phi_d^{r,0}(K) := \frac{1}{r!} \int_K x^r dx, \quad (2.5)$$

and by

$$\Phi_k^{r,s}(K) := 0 \quad \text{if } k \notin \{0, \dots, d\} \text{ or } r \notin \mathbb{N}_0 \text{ or } s \notin \mathbb{N}_0 \text{ or } k = d, s \neq 0.$$

Note that the tensor product $x^r u^s$ in the integrand is the symmetric tensor product of the symmetric tensor powers x^r and u^s .

Minkowski tensors can be defined not only for convex bodies or compact sets with positive reach. By additivity their domain can be extended to the class of polyconvex sets (finite unions of convex bodies). Moreover they can be defined also for sets from the class \mathcal{U}^d , since this generalization is also true for the support measures. Furthermore, Minkowski tensors can be introduced for even more general classes of sets provided that the support measures are defined in a natural way and the integrals exist (see Section 3 and the references given there). An explicit description of the Minkowski tensors of polytopes is recalled in Section 4.4, in Section 4.5 we evaluate formulas for nonconvex sets. In the case of sets with positive reach or for even more general classes of compact sets K (such as arbitrary finite unions of sets with positive reach), the support measures $\Lambda_j(K, \cdot)$ are consistently replaced by the reach measures $\mu_j(K; \cdot)$ in definition (2.4); the relationship between these measures will be discussed in Section 3.

It is a straightforward consequence of the properties of the support measures of convex bodies that the Minkowski tensors of convex bodies are continuous, isometry (rigid motion) covariant (for a detailed definition, especially of the underlying notion of polynomial behavior with respect to translations, we refer to [25, Section 2.2]) and additive tensor functionals (valuations) on the space of convex bodies in \mathbb{R}^d . By a fundamental result due to Alesker, the vector space T_p of all mappings $\Gamma : \mathcal{K}^d \rightarrow \mathbb{T}^p$ having these properties is spanned by the tensor valuations $Q^m \Phi_k^{r,s}$, where $m, r, s \in \mathbb{N}_0$ satisfy $2m + r + s = p$, where $k \in \{0, \dots, d\}$, and where $s = 0$ if $k = d$. In contrast to the real-valued and vector-valued case, these tensor valuations are no longer linearly independent. A study of linear dependencies was initiated by McMullen and completed by Hug, Schneider, Schuster (for precise references and detailed statements, see, e.g., [25, Thms. 2.6 and 2.7]). These general investigations imply that if $T_{2,k}$ denotes the subspace of all maps in T_2 that are homogeneous of degree k , then $T_2 = T_{2,0} \oplus \dots \oplus T_{2,d+2}$ (direct sum decomposition), $\dim T_2 = 3d + 1$, and a basis of $T_{2,k}$ is displayed in Table 1. Denoting by T_2^* the subspace of translation invariant maps in T_2 and by $T_{2,k}^*$ the subspace of translation invariant maps in $T_{2,k}$, we have $T_2^* = T_{2,0}^* \oplus \dots \oplus T_{2,d}^*$, $\dim T_2^* = 2d$, and a basis of $T_{2,k}^*$ is displayed in Table 1.

Table 1: Bases for the subspaces $T_{2,k}$, $k \in \{0, \dots, d+2\}$, and $T_{2,k}^*$, $k \in \{0, \dots, d\}$

	$k = 0$	$k = 1$	$k \in \{2, \dots, d-1\}$	$k = d$	$k \in \{d+1, d+2\}$
$T_{2,k}$	$\{Q\Phi_0^{0,0}\}$	$\{\Phi_1^{0,2}, Q\Phi_1^{0,0}\}$	$\{\Phi_k^{0,2}, Q\Phi_k^{0,0}, \Phi_{k-2}^{2,0}\}$	$\{\Phi_{d-2}^{2,0}, Q\Phi_d^{0,0}\}$	$\{Q\Phi_{k-2}^{2,0}\}$
$T_{2,k}^*$	$\{Q\Phi_0^{0,0}\}$	$\{\Phi_1^{0,2}, Q\Phi_1^{0,0}\}$	$\{\Phi_k^{0,2}, Q\Phi_k^{0,0}\}$	$\{Q\Phi_d^{0,0}\}$	–

3 Asymptotics for estimators: a theoretical foundation

Let $A \subset \mathbb{R}^d$ be a nonempty closed set. The topological boundary of A is denoted by ∂A . The (positive) normal bundle of A is the subset of $\mathbb{R}^d \times \mathbb{S}^{d-1}$ which is defined by

$$\text{Nor}(A) := \{(x, u) \in \partial A \times \mathbb{S}^{d-1} : \text{dist}(A, x + ru) = r \text{ for some } r > 0\}$$

and the reach function of A is given by

$$r_A(x, u) := \sup\{s > 0 : \text{dist}(A, x + su) = s\}, \quad (x, u) \in \text{Nor}(A)$$

(note the slight correction in comparison with [23], see also [24]). In the following, we write \mathcal{H}^k for the k -dimensional Hausdorff measure for $k \in \{0, \dots, d\}$. We remark that A has reach at least $r > 0$ if $r_A(x, u) \geq r$ for \mathcal{H}^{d-1} -almost all $(x, u) \in \text{Nor}(A)$; see [24, Lemma 3.19] for a more general fact.

It was shown in [23, Theorem 2.1], [24, Theorem 3.16] that there exist uniquely determined signed “reach measures” $\mu_i(A; \cdot)$ on $\mathbb{R}^d \times \mathbb{S}^{d-1}$, for $i \in \{0, \dots, d-1\}$, concentrated on $\text{Nor}(A)$ and such that

$$\begin{aligned} & \int_{\mathbb{R}^d \setminus A} f(z) \mathcal{H}^d(dz) \\ &= \sum_{i=0}^{d-1} \omega_{d-i} \int_0^\infty \int_{\text{Nor}(A)} t^{d-1-i} \mathbb{1}\{r_A(x, u) > t\} f(x + tu) \mu_i(A; d(x, u)) dt, \end{aligned} \quad (3.1)$$

where $f : \mathbb{R}^d \rightarrow \mathbb{R}$ is an arbitrary measurable bounded function with compact support. Clearly, (3.1) remains true if f takes values in the (finite-dimensional) vector space $\mathbb{T}^r(\mathbb{R}^d)$, for any fixed $r \in \mathbb{N}_0$, where $f : \mathbb{R}^d \rightarrow \mathbb{T}^r(\mathbb{R}^d)$ is said to be bounded if the map $x \mapsto |f(x)|$ is bounded (f is bounded on a subset B if the restriction of this map to B is bounded).

Remark 3.1. If $A \in \mathcal{U}^d$, then the support measures $\Lambda_j(A, \cdot)$ of A are defined by additive extension. For this generalization it is crucial that A can be obtained as a finite union of compact sets A_i with positive reach, $i \in \{1, \dots, m\}$, such that arbitrary finite intersections of these sets have again positive reach (compare [49, Example 4.16]). It was shown in [23, Section 3] that

$$\mu_j(A; \cdot) = \Lambda_j(A, \text{Nor}(A) \cap \cdot), \quad \text{for } j = 0, \dots, d-1.$$

Moreover, the arguments in [23, Sections 3 and 4] show that indeed

$$\mu_{d-1}(A; \cdot) = \Lambda_{d-1}(A, \cdot) \quad (3.2)$$

as Borel measures on $\mathbb{R}^d \times \mathbb{S}^{d-1}$; see also [48, Corollary 2]. In particular, $A \mapsto \mu_{d-1}(A; \cdot)$ is additive on \mathcal{U}^d . On the other hand, the support measures are in general not defined on the larger domain of finite unions of sets with positive reach. For this reason, we work with the reach measures whenever the support measures are not available. Relation (3.2) shows that this approach is consistent with the previous literature if we restrict ourselves to the top order measures with index $j = d - 1$ as in definition (4.2) below.

The integrals on the right-hand side of (3.1) are well defined, but in general the reach measures $\mu_i(A; \cdot)$ are not Radon measures. In the following, we consider compact sets $A \subset \mathbb{R}^d$ and assume that the (nonnegative) total variation measure $\|\mu_i(A)\|(\cdot)$ of $\mu_i(A; \cdot)$ is finite for $i \in \{0, \dots, d - 1\}$. A sufficient condition is provided in Lemma 3.2.

Lemma 3.2. *If A is a finite union of compact sets of positive reach, then the total variation measures of the reach measures of A are concentrated on $\text{Nor}(A)$ and satisfy*

$$\|\mu_i(A)\|(\mathbb{R}^d \times \mathbb{S}^{d-1}) < \infty \quad \text{for } i \in \{0, \dots, d - 1\}. \quad (3.3)$$

Proof. Recall that $\mu_i(A; \cdot)$ is concentrated on $\text{Nor}(A)$ which implies the first assertion of the lemma.

It follows from [23, Corollary 2.5] that

$$\|\mu_i(A)\|(\text{Nor}(A)) \leq c(d, i) \int_{\text{Nor}(A)} |H_{d-1-i}(A, x, u)| \mathcal{H}^{d-1}(d(x, u)),$$

where $c(d, i)$ is a finite constant and $|H_{d-1-i}(A, x, u)| \leq \binom{d-1}{i}$, as can be seen from [23, (2.13)]. Let $A = \bigcup_{i=1}^m A_i$ with compact sets A_i with positive reach. It is well known that $\text{Nor}(A_i)$ is bilipschitz homeomorphic to the compact submanifold $\text{dist}(A_i, \cdot)^{-1}(\{r_0\})$, if r_0 is smaller than the reach of A_i . Hence $\mathcal{H}^{d-1}(\text{Nor}(A_i)) < \infty$. Since

$$\text{Nor}(A) \subset \bigcup_{i=1}^m \text{Nor}(A_i),$$

the assertion follows. \square

Let $A \subset \mathbb{R}^d$ be a nonempty closed set. For \mathcal{H}^d -almost all $z \in \mathbb{R}^d \setminus A$, the metric projection $p_A(z) \in A$ to A and the vector $u_A(z) \in \mathbb{S}^{d-1}$ are uniquely determined by

$$\|p_A(z) - z\| = \text{dist}(A, z) := \min\{\|a - z\| : a \in A\}, \quad u_A(z) = \frac{z - p_A(z)}{\text{dist}(A, z)}.$$

Note that $p_A(z) = z$ for $z \in A$, and if $(x, u) \in \text{Nor}(A)$ and $0 < s < r_A(x, u)$, then $p_A(x + su) = x$ and $u_A(x + su) = u$. If A is a nonempty compact set, we consider

$$\partial^+ A := \{x \in \partial A : (x, u) \in \text{Nor}(A) \text{ for some } u \in \mathbb{S}^{d-1}\},$$

and for $x \in \partial^+ A$ we define the set of unit normal vectors of A at x by

$$N(A, x) := \{u \in \mathbb{S}^{d-1} : (x, u) \in \text{Nor}(A)\}.$$

Note that $N(A, x)$ is either a singleton, consists of two unit vectors $\{\pm u\}$ or is an (infinite) spherically convex set. Then we set

$$\partial^i A := \{x \in \partial^+ A : |N(A, x)| = i\}, \quad i \in \{1, 2\}.$$

We write $\nu_A(x)$ for the unique unit vector in $N(A, x)$, for $x \in \partial^1 A$, and $\pm\nu_A(x)$ for the two unit vectors in $N(A, x)$, if $x \in \partial^2 A$. For $\varepsilon > 0$, let $A^\varepsilon := \{x \in \mathbb{R}^d : \text{dist}(A, x) \leq \varepsilon\}$ denote the ε neighborhood of A .

Theorem 3.3. *Let $r, s \in \mathbb{N}_0$. Let $A \subset \mathbb{R}^d$ be a nonempty compact set such that (3.3) holds. If $f : \mathbb{R}^d \rightarrow \mathbb{T}^r(\mathbb{R}^d)$ is measurable and bounded on ∂A , then*

$$\begin{aligned} & \lim_{\varepsilon \rightarrow 0_+} \frac{1}{\varepsilon} \int_{A^\varepsilon \setminus A} f(p_A(z)) u_A(z)^s \mathcal{H}^d(dz) \\ &= \int_{\partial^1 A} f(x) \nu_A(x)^s \mathcal{H}^{d-1}(dx) + (1 + (-1)^s) \int_{\partial^2 A} f(x) \nu_A(x)^s \mathcal{H}^{d-1}(dx). \end{aligned}$$

In particular, the assertion holds for finite unions of compact sets with positive reach.

Proof. We apply (3.1) with the map $\tilde{f} : \mathbb{R}^d \rightarrow \mathbb{T}^{r+s}$, $\tilde{f}(z) = f(p_A(z)) u_A(z)^s \mathbf{1}\{z \in A^\varepsilon \setminus A\}$, which yields

$$\begin{aligned} & \int_{A^\varepsilon \setminus A} f(p_A(z)) u_A(z)^s \mathcal{H}^d(dz) \\ &= \sum_{i=0}^{d-1} \omega_{d-i} \int_0^\varepsilon \int_{\text{Nor}(A)} t^{d-1-i} f(x) u^s \mathbf{1}\{r_A(x, u) > t\} \mu_i(A; d(x, u)) dt. \end{aligned}$$

We consider

$$h_i(t) := \omega_{d-i} t^{d-1-i} \int_{\text{Nor}(A)} f(x) u^s \mathbf{1}\{r_A(x, u) > t\} \mu_i(A; d(x, u)).$$

If $i \in \{0, \dots, d-2\}$, then

$$\begin{aligned} \varepsilon^{-1} \left| \int_0^\varepsilon h_i(t) dt \right| &\leq \frac{\omega_{d-i}}{\varepsilon} \int_0^\varepsilon t^{d-1-i} \int_{\text{Nor}(A)} |f(x)| \mathbf{1}\{r_A(x, u) > t\} \|\mu_i(A)\| d(x, u) dt \\ &\leq \frac{\omega_{d-i}}{d-i} \cdot |f|_{\partial A} \cdot \|\mu_i(A)\| (\text{Nor}(A)) \cdot \varepsilon^{d-i-1} \rightarrow 0 \quad \text{as } \varepsilon \rightarrow 0_+, \end{aligned}$$

where $|f|_{\partial A} := \sup\{|f(x)| : x \in \partial A\} < \infty$ and basic properties of the norm $|\cdot|$ on (symmetric) tensors were used, in particular (2.2). Moreover, by the dominated convergence theorem,

$$\begin{aligned} h_{d-1}(t) &= 2 \int_{\text{Nor}(A)} f(x) u^s \mathbf{1}\{r_A(x, u) > t\} \mu_{d-1}(A; d(x, u)) \\ &\rightarrow 2 \int_{\text{Nor}(A)} f(x) u^s \mu_{d-1}(A; d(x, u)) =: h_{d-1}(0_+) \quad \text{as } t \rightarrow 0_+, \end{aligned}$$

since $r_A(x, u) > 0$ for $(x, u) \in \text{Nor}(A)$. Note that by [23, Proposition 4.1], $\mu_{d-1}(A; \cdot)$ is nonnegative and

$$\begin{aligned} 2\mu_{d-1}(A; \cdot) &= \int_{\partial^1 A} \mathbf{1}\{(x, \nu_A(x)) \in \cdot\} \mathcal{H}^{d-1}(dx) \\ &\quad + \int_{\partial^2 A} \mathbf{1}\{(x, \nu_A(x)) \in \cdot\} + \mathbf{1}\{(x, -\nu_A(x)) \in \cdot\} \mathcal{H}^{d-1}(dx). \end{aligned} \tag{3.4}$$

Hence, if $t \rightarrow 0_+$, then

$$h_{d-1}(t) \rightarrow \int_{\partial^1 A} f(x) \nu_A(x)^s \mathcal{H}^{d-1}(dx) + (1 + (-1)^s) \int_{\partial^2 A} f(x) \nu_A(x)^s \mathcal{H}^{d-1}(dx).$$

Since

$$\varepsilon^{-1} \int_0^\varepsilon h_{d-1}(t) dt \rightarrow h_{d-1}(0_+) \quad \text{as } \varepsilon \rightarrow 0_+,$$

the assertion follows. \square

By essentially the same argument, we obtain the following variant of Theorem 3.3. The case $s = 0$ of the next theorem is already covered by Theorem 3.3 with the domain of integration restricted to the complement of the set A .

Theorem 3.4. *Let $s \in \mathbb{N}$. Let $A \subset \mathbb{R}^d$ be a nonempty compact set such that (3.3) holds. If $f : \mathbb{R}^d \rightarrow \mathbb{T}^r(\mathbb{R}^d)$ is measurable and bounded on ∂A , then*

$$\begin{aligned} & \lim_{\varepsilon \rightarrow 0_+} \frac{1+s}{\varepsilon^{1+s}} \int_{A^\varepsilon} f(p_A(z))(z - p_A(z))^s \mathcal{H}^d(dz) \\ &= \int_{\partial^1 A} f(x) \nu_A(x)^s \mathcal{H}^{d-1}(dx) + (1 + (-1)^s) \int_{\partial^2 A} f(x) \nu_A(x)^s \mathcal{H}^{d-1}(dx). \end{aligned} \quad (3.5)$$

In particular, the assertion holds for finite unions of compact sets with positive reach.

Proof. First, note that $z - p_A(z) = o$ if $z \in A$ and $s \neq 0$. Hence the domain of integration on the left-hand side can be restricted to $A^\varepsilon \setminus A$ without changing the value of the integral. We apply (3.1) with the map $\hat{f} : \mathbb{R}^d \rightarrow \mathbb{T}^{r+s}$, $\hat{f}(z) = f(p_A(z))(z - p_A(z))^s \mathbf{1}\{z \in A^\varepsilon \setminus A\}$ and use that $(x + tu) - p_A(x + tu) = tu$ for $(x, u) \in \text{Nor}(A)$ and $0 < t < r_A(x, u)$. Thus we obtain

$$\begin{aligned} & \int_{A^\varepsilon} f(p_A(z))(z - p_A(z))^s \mathcal{H}^d(dz) \\ &= \sum_{i=0}^{d-1} \omega_{d-i} \int_0^\varepsilon \int_{\text{Nor}(A)} t^{d-1-i+s} f(x) u^s \mathbf{1}\{r_A(x, u) > t\} \mu_i(A; d(x, u)) dt. \end{aligned}$$

Note that if $g : [0, \infty) \rightarrow \mathbb{R}$ is measurable and bounded, and $g(t) \rightarrow g(0_+)$ as $t \rightarrow 0_+$, then

$$\varepsilon^{-(1+s)} \int_0^\varepsilon t^s g(t) dt \rightarrow \frac{g(0_+)}{1+s} \quad \text{as } \varepsilon \rightarrow 0_+.$$

Otherwise, the proof follows the lines of the proof of Theorem 3.3. \square

4 Algorithms to estimate Minkowski tensors

In this section, we define explicit algorithms that are used to estimate the Minkowski tensors, given a discrete (pixelated) data set. We focus on the current improvements in comparison to the original algorithm suggested in [21]. The digitized estimator of the volume tensors and especially the least squares fit with respect to the radial dependence strongly improve the robustness of the algorithm. Then we discuss details of our open-source implementation [47] and provide some advice on the choice of parameters. Finally, we demonstrate the performance for some test cases; see Sections 4.4 and 4.5.

4.1 Description and analysis

In the following, we describe two methods for estimating Minkowski tensors. The first is based on Corollary 4.1 and works for arbitrary finite unions of compact sets with positive reach and (surface) tensor functionals $\Phi_{d-1}^{r,s}$ with $s \geq 1$. The second approach, which is applicable for arbitrary tensor functionals $\Phi_j^{r,s}$, is based on solving a least squares problem and offers practical advantages. However, its theoretical foundation is only available for sets with positive reach. Nevertheless, in Section 4.5, we will see that it provides surprisingly accurate results for a set without positive reach.

To explain the two approaches, we fix integers $r, s \in \mathbb{N}_0$. The Voronoi tensor $\mathcal{V}_R^{r,s}(K)$ with distance parameter $R \geq 0$ and rank parameter tuple $(r, s) \in \mathbb{N}_0^2$ of a nonempty compact set $K \subset \mathbb{R}^d$ is defined by

$$\mathcal{V}_R^{r,s}(K) := \int_{K^R} p_K(x)^r (x - p_K(x))^s \mathcal{H}^d(dx), \quad (4.1)$$

where K^R is the set of points with distance at most $R > 0$ from K and p_K is the (almost everywhere uniquely defined) metric projection on K . For $r = s = 0$ the Voronoi tensor with distance parameter R is the volume of K^R , i.e., the volume of the set of points with distance at most R from K .

The following corollary of Theorem 3.4 shows how surface tensors can be approximated by Voronoi tensors. Recall the definition of the reach measure $\mu_{d-1}(A; \cdot)$ of a nonempty compact subset of \mathbb{R}^d from Section 3, which equals the support measure $\Lambda_{d-1}(A, \cdot)$ if $A \in \mathcal{U}^d$ (see Remark 3.1 which ensures that the Minkowski tensor $\Phi_{d-1}^{r,s}$ in (4.2) is consistently defined for all $r, s \in \mathbb{N}_0$). An explicit description of the reach measure $\mu_{d-1}(A; \cdot)$ is provided in (3.4) (see [23, Proposition 4.1]).

Corollary 4.1. *Let $K \subset \mathbb{R}^d$ be a finite union of compact sets of positive reach. If $r \in \mathbb{N}_0$ and $s \in \mathbb{N}$, then*

$$\lim_{\varepsilon \rightarrow 0^+} \frac{1}{\varepsilon^{1+s}} \mathcal{V}_\varepsilon^{r,s}(K) = r!s! \kappa_{s+1} \Phi_{d-1}^{r,s}(K)$$

and

$$\lim_{\varepsilon \rightarrow 0^+} \frac{1}{\varepsilon} \left(\mathcal{V}_\varepsilon^{r,0}(K) - \mathcal{V}_{\varepsilon^2}^{r,0}(K) \right) = r!2 \Phi_{d-1}^{r,0}(K),$$

where, for $r, s \in \mathbb{N}_0$,

$$\Phi_{d-1}^{r,s}(K) := \frac{1}{r!s!} \frac{2}{\omega_{1+s}} \int_{\mathbb{R}^d \times \mathbb{S}^{d-1}} x^r u^s \mu_{d-1}(K; d(x, u)). \quad (4.2)$$

Proof. First, we consider the case where $s \in \mathbb{N}$. We apply Theorem 3.4 with $f(x) = x^r$, $x \in \mathbb{R}^d$. Using the definition (4.1) of the total Voronoi tensor measure, we get the required expression on the left-hand side, after division by $1 + s$. Accordingly, the right-hand side of equation (3.5) turns into

$$\frac{2}{s+1} \int x^r u^s \mu_{d-1}(K; d(x, u)),$$

where also relation (3.4) was used. The assertion now follows from the definition of the Minkowski tensor $\Phi_{d-1}^{r,s}(K)$.

If $s = 0$, then an application of Theorem 3.3 and relation (3.4) yield

$$\begin{aligned} \lim_{\varepsilon \rightarrow 0_+} \frac{1}{\varepsilon} \left(\mathcal{V}_\varepsilon^{r,0}(K) - \mathcal{V}_{\varepsilon^2}^{r,0}(K) \right) &= \lim_{\varepsilon \rightarrow 0_+} \frac{1}{\varepsilon} \left(\mathcal{V}_\varepsilon^{r,0}(K) - \mathcal{V}_0^{r,0}(K) \right) - \lim_{\varepsilon \rightarrow 0_+} \frac{\varepsilon}{\varepsilon^2} \left(\mathcal{V}_{\varepsilon^2}^{r,0}(K) - \mathcal{V}_0^{r,0}(K) \right) \\ &= 2r! \Phi_{d-1}^{r,0}(K) - 0, \end{aligned}$$

which proves the assertion. \square

For a finite set $K_0 \subset \mathbb{R}^d$ and $r, s \in \mathbb{N}_0$, the Voronoi tensors simplify to

$$\mathcal{V}_R^{r,s}(K_0) = \sum_{x \in K_0} x^r \int_{B(x,R) \cap V_x(K_0)} (y-x)^s \mathcal{H}^d(dy), \quad (4.3)$$

where $B(x, R)$ is the closed ball with center x and radius R and

$$V_x(K_0) := \{y \in \mathbb{R}^d : p_{K_0}(y) = x\}$$

is the Voronoi cell of $x \in K_0$ with respect to the set K_0 . It is clear that each compact set $K \subset \mathbb{R}^d$ can be approximated with any specified precision by finite sets $K_0 \subset \mathbb{R}^d$ with respect to the Hausdorff metric d_H on compact subsets of \mathbb{R}^d (see, e.g., (4.10)). If $K, K_0 \subseteq B(o, \rho)$ for some $\rho > 0$, then

$$|\mathcal{V}_R^{r,s}(K) - \mathcal{V}_R^{r,s}(K_0)| \leq C(d, R, \rho, r, s) \cdot d_H(K, K_0)^{\frac{1}{2}}, \quad (4.4)$$

which follows from [21, Thm. 4.1], where $C(d, R, \rho, r, s)$ is a constant depending only on the arguments in brackets. An inspection of the proof of Theorem 4.1 in [21] shows that the constant $C(d, R, \rho, r, s)$ can be chosen such that $C(d, R, \rho, r, s) \leq C(d, R_0, \rho, r, s)$ if $0 < R \leq R_0$. Note that (4.4) does not require that K_0 is a subset of K (although an approximation of K from inside can be guaranteed for a given K) and holds whenever K, K_0 are compact subsets of $B(o, \rho)$. Recall from [21] that $d_H(K, K_0)^{\frac{1}{2}}$ can be replaced by $d_H(K, K_0)$ if $r = s = 0$.

Evaluating the integral in (4.3) can be cumbersome and inefficient. Moreover, we do not require a precision beyond the approximation of K via K_0 . We, therefore, estimate the Voronoi tensors in (4.3) by considering a random grid

$$\eta = \sum_{z \in a \cdot \mathbb{Z}^d} \delta_{z+U_a} \quad (4.5)$$

with some scaling parameter $a > 0$ and a uniform random vector $U_a \sim \mathcal{U}([0, a]^d)$. The tensor-valued random variable

$$\widehat{\mathcal{V}}_R^{r,s}(K_0, a) = a^d \sum_{x \in \eta} \mathbb{1}\{\|x - p_{K_0}(x)\| < R\} p_{K_0}(x)^r (x - p_{K_0}(x))^s \quad (4.6)$$

will then be used as an estimator for $\mathcal{V}_R^{r,s}(K_0)$. Since K_0 is a finite set, only finitely many summands do not vanish. The estimated Voronoi tensor in (4.6) can be viewed as a discrete version of the integral in (4.3). Figure 1 (a) provides an example data set K_0 , which is given as a finite subset of an underlying set with positive reach. In Figure 1 (b) the idea of the estimator (4.6) is demonstrated for this example data set K_0 . For each data point $x \in K_0$ one can see the Voronoi cell $V_x(K_0)$.

Lemma 4.2. *Let $K_0 \subset \mathbb{R}^d$ be a finite set and $a > 0$. Then the estimator $\widehat{\mathcal{V}}_R^{r,s}(K_0, a)$ for $\mathcal{V}_R^{r,s}(K_0)$ is unbiased, that is, $\mathbb{E}\widehat{\mathcal{V}}_R^{r,s}(K_0, a) = \mathcal{V}_R^{r,s}(K_0)$.*

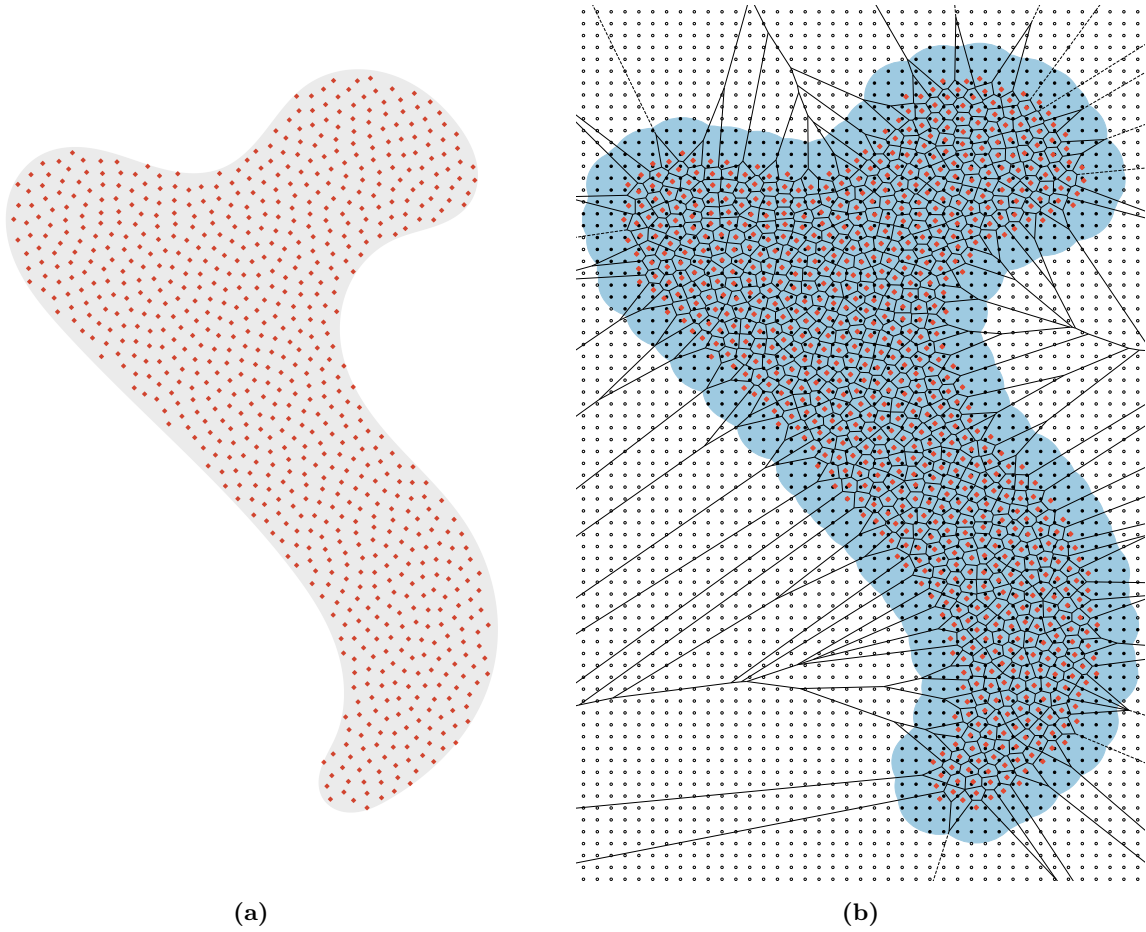


Figure 1: Example data K_0 (red points), which is a finite subset of an underlying set with positive reach (a), and the Voronoi diagram (b) of the data K_0 and the set K_0^R (blue) of points with distance not bigger than some $R > 0$ from K_0 . The algorithm uses a random grid η (compare (4.6)) to estimate the Voronoi tensor $\mathcal{V}_R^{r,s}(K_0)$ of K_0 , where only the points of η inside K_0^R are relevant for the estimation.

Proof. Let $\{z_i : i \in \mathbb{N}\} = a \cdot \mathbb{Z}^d$ be an enumeration of the points in the lattice $a \cdot \mathbb{Z}^d$. Then

$$\begin{aligned} \widehat{\mathcal{V}}_R^{r,s}(K_0, a) &= a^d \sum_{i \geq 1} \mathbf{1}\{\|z_i + U_a - p_{K_0}(z_i + U_a)\| < R\} p_{K_0}(z_i + U_a)^r (z_i + U_a - p_{K_0}(z_i + U_a))^s \\ &= a^d \sum_{i \geq 1} \sum_{w \in K_0} \mathbf{1}\{p_{K_0}(z_i + U_a) = w\} \mathbf{1}\{\|z_i + U_a - w\| < R\} w^r (z_i + U_a - w)^s. \end{aligned}$$

Note that $p_{K_0}(z_i + U_a)$ is uniquely defined \mathbb{P} -almost surely, since U_a has a density with respect to the Lebesgue measure.

If the indicator functions are nonzero, then for every $i \in \mathbb{N}$ there is some $w \in K_0$ such that $\|z_i + U_a - w\| \leq R$, and hence $z_i \in K_0 + B(\sqrt{d}a + R)$. In particular, this shows that the effective ranges of the summations over $i \geq 1$ and $w \in K_0$ are finite and can be chosen independently of U_a . Moreover, (2.2) yields

$$|w^r (z_i + U_a - w)^s| \leq \|w\|^r \cdot \|z_i + U_a - w\|^s \leq C(K_0)^r R^s < \infty,$$

where $C(K_0)$ is a constant that depends only on K_0 , but not on a specific $w \in K_0$.

These remarks allow us to interchange summation and expectation so that

$$\begin{aligned}
\mathbb{E}\widehat{\mathcal{V}}_R^{r,s}(K_0, a) &= a^d \sum_{i \geq 1} \sum_{w \in K_0} \mathbb{E} \mathbf{1}\{p_{K_0}(z_i + U_a) = w\} \mathbf{1}\{\|z_i + U_a - w\| < R\} w^r (z_i + U_a - w)^s \\
&= \sum_{w \in K_0} \sum_{i \geq 1} \int_{z_i + [0, a]^d} \mathbf{1}\{p_{K_0}(y) = w\} \mathbf{1}\{\|y - w\| < R\} w^r (y - w)^s \mathcal{H}^d(dy) \\
&= \sum_{w \in K_0} \int_{\mathbb{R}^d} \mathbf{1}\{y \in V_w(K_0)\} \mathbf{1}\{\|y - w\| < R\} w^r (y - w)^s \mathcal{H}^d(dy) \\
&= \sum_{w \in K_0} w^r \int_{\mathbb{R}^d} \mathbf{1}\{y \in V_w(K_0) \cap B(w, R)\} (y - w)^s \mathcal{H}^d(dy) = \mathcal{V}_R^{r,s}(K_0),
\end{aligned}$$

which proves the assertion. \square

Next we show that $\widehat{\mathcal{V}}_R^{r,s}(K_0, a)$ is a consistent estimator for $\mathcal{V}_R^{r,s}(K)$, as $K_0 \rightarrow K$ in the Hausdorff metric and $a = a(K_0) \rightarrow 0$. More precisely, we obtain the following quantitative estimate. We write

$$\mathbf{N}(K_0) = \min\{\|x_1 - x_2\| : x_1, x_2 \in K_0, x_1 \neq x_2\}$$

for the minimal distance of any two different points in a finite set $K_0 \subset \mathbb{R}^d$ of cardinality at least two (which we tacitly assume all the time) and $s \wedge t$ for the minimum of $s, t \in \mathbb{R}$.

Theorem 4.3. *Let $K \subset \mathbb{R}^d$ be a compact set, let $r, s \in \mathbb{N}_0$ and $R > 0$. Let $\rho > 0$ be such that $K \subseteq B(o, \rho)$. If $K_0 \subseteq B(o, \rho)$ is a finite set and $a > 0$, then almost surely*

$$|\widehat{\mathcal{V}}_R^{r,s}(K_0, a) - \mathcal{V}_R^{r,s}(K)| \leq C'(d, R, \rho, r, s) \left(d_H(K, K_0)^{\frac{1}{2}} + \max \left\{ \frac{a}{\mathbf{N}(K_0)}, \left(\frac{a}{\mathbf{N}(K_0)} \right)^d \right\} \right),$$

where $C'(d, R, \rho, r, s)$ is a positive constant, and $d_H(K, K_0)^{\frac{1}{2}}$ can be replaced by $d_H(K, K_0)$ if $r = s = 0$.

In particular, if $(K_0(i))_{i \in \mathbb{N}}$ is a sequence of finite sets in \mathbb{R}^d and $(a_i)_{i \in \mathbb{N}}$ is a sequence of positive numbers such that $K_0(i) \rightarrow K$ in the Hausdorff metric and $\mathbf{N}(K_0(i))^{-1} a_i \rightarrow 0$, as $i \rightarrow \infty$, then $\widehat{\mathcal{V}}_R^{r,s}(K_0(i), a_i) \rightarrow \mathcal{V}_R^{r,s}(K)$, as $i \rightarrow \infty$, almost surely.

Proof. The constants employed in the proof are denoted by c, c_1, c_2 and depend only the parameters indicated in brackets.

By the triangle inequality and in view of (4.4) it is sufficient to show that for a fixed finite set K_0 , almost surely we have

$$|\widehat{\mathcal{V}}_R^{r,s}(K_0, a) - \mathcal{V}_R^{r,s}(K_0)| \leq c(d, R, \rho, r, s) \cdot \max \left\{ \frac{a}{\mathbf{N}(K_0)}, \left(\frac{a}{\mathbf{N}(K_0)} \right)^d \right\}.$$

For this, observe that almost surely $p_{K_0}(z + U_a)$ is uniquely defined for each $z \in a \cdot \mathbb{Z}^d$. Hence,

almost surely

$$\begin{aligned}
\widehat{\mathcal{V}}_R^{r,s}(K_0, a) &= a^d \sum_{z \in a \cdot \mathbb{Z}^d} \mathbf{1}\{\|z + U_a - p_{K_0}(z + U_a)\| < R\} p_{K_0}(z + U_a)^r (z + U_a - p_{K_0}(z + U_a))^s \\
&= \sum_{x \in K_0} a^d \sum_{z \in a \cdot \mathbb{Z}^d} \mathbf{1}\{\|z + U_a - x\| < R\} \mathbf{1}\{z + U_a \in V_x(K_0)\} x^r (z + U_a - x)^s \\
&= \sum_{x \in K_0} x^r \sum_{z \in a \cdot \mathbb{Z}^d} \mathbf{1}_{B(x,R) \cap V_x(K_0)}(z + U_a) (z + U_a - x)^s a^d \\
&= \sum_{x \in K_0} x^r \int \sum_{z \in a \cdot \mathbb{Z}^d} \mathbf{1}_{B(x,R) \cap V_x(K_0)}(z + U_a) (z + U_a - x)^s \mathbf{1}_{z+[0,a]^d}(y) \mathcal{H}^d(dy).
\end{aligned}$$

Note that in the last step integration and summation can be interchanged, since for each $x \in K_0$ there are only finitely many summands $z \in a \cdot \mathbb{Z}^d$ such that the first indicator is nonzero. Moreover, we have

$$\begin{aligned}
\mathcal{V}_R^{r,s}(K_0) &= \sum_{x \in K_0} x^r \int \mathbf{1}_{B(x,R) \cap V_x(K_0)}(y) (y - x)^s \mathcal{H}^d(dy) \\
&= \sum_{x \in K_0} x^r \int \sum_{z \in a \cdot \mathbb{Z}^d} \mathbf{1}_{B(x,R) \cap V_x(K_0)}(y) (y - x)^s \mathbf{1}_{z+[0,a]^d}(y) \mathcal{H}^d(dy).
\end{aligned}$$

Hence, using (2.2), we get

$$\begin{aligned}
&|\widehat{\mathcal{V}}_R^{r,s}(K_0, a) - \mathcal{V}_R^{r,s}(K_0)| \\
&\leq \rho^r \sum_{x \in K_0} \int \sum_{z \in a \cdot \mathbb{Z}^d} |\mathbf{1}_{B(x,R) \cap V_x(K_0)}(z + U_a) (z + U_a - x)^s - \mathbf{1}_{B(x,R) \cap V_x(K_0)}(y) (y - x)^s| \\
&\quad \times \mathbf{1}_{z+[0,a]^d}(y) \mathcal{H}^d(dy).
\end{aligned}$$

If $z + [0, a]^d \subseteq B(x, R) \cap V_x(K_0)$, then (2.2) and (2.3) shows that the expression $|\cdot|$ under the integral can be bounded from above by

$$|(z + U_a - x)^s - (y - x)^s| \leq s \cdot \|z + U_a - y\| \cdot R^{s-1} \leq s \cdot \sqrt{d} R^{s-1} \cdot a.$$

If $(z + [0, a]^d) \cap B(x, R) \cap V_x(K_0) = \emptyset$, then the expression is zero. In the remaining case, we have $(z + [0, a]^d) \cap \partial(B(x, R) \cap V_x(K_0)) \neq \emptyset$ and the expression $|\cdot|$ is bounded from above by $2R^s$ (see (2.2)). Thus we obtain

$$\begin{aligned}
&|\widehat{\mathcal{V}}_R^{r,s}(K_0, a) - \mathcal{V}_R^{r,s}(K_0)| \\
&\leq \rho^r \sum_{x \in K_0} \left(\sum_{z \in a \cdot \mathbb{Z}^d} \mathbf{1}\{z + [0, a]^d \subseteq B(x, R) \cap V_x(K_0)\} \cdot s \cdot \sqrt{d} R^{s-1} \cdot a \cdot a^d \right. \\
&\quad \left. + \sum_{z \in a \cdot \mathbb{Z}^d} \mathbf{1}\{(z + [0, a]^d) \cap \partial(B(x, R) \cap V_x(K_0)) \neq \emptyset\} \cdot 2R^s \cdot a^d \right) \\
&\leq d \rho^r R^{s-1} \sum_{x \in K_0} \left(s \cdot a \mathcal{H}^d(B(x, R) \cap V_x(K_0)) \right. \\
&\quad \left. + R \mathcal{H}^d(\partial(B(x, R) \cap V_x(K_0)) + B(o, \sqrt{d} \cdot a)) \right)
\end{aligned}$$

$$\begin{aligned} &\leq s \cdot d\rho^r R^{s-1} \cdot a \cdot \mathcal{H}^d(K + B(o, d_H(K, K_0) + R)) \\ &\quad + d\rho^r R^s \sum_{x \in K_0} \mathcal{H}^d\left(\partial(B(x, R) \cap V_x(K_0)) + B(o, \sqrt{d} \cdot a)\right), \end{aligned} \quad (4.7)$$

where we used that the Voronoi cells have pairwise disjoint interiors. Since $K, K_0 \subset B(o, \rho)$, we get

$$\mathcal{H}^d(K + B(o, d_H(K, K_0) + R)) \leq \mathcal{H}^d(B(o, 2\rho + R)) \leq \kappa_d(2\rho + R)^d. \quad (4.8)$$

To deal with the remaining sum, we denote by r_x the inradius of the Voronoi cell $V_x(K_0)$. Using a volume bound from the proof of Lemma 3.6 in [22] and the obvious inequality $r_x \geq \mathbf{N}(K_0)/2$ for $x \in K_0$, we obtain

$$\begin{aligned} &\mathcal{H}^d\left(\partial(B(x, R) \cap V_x(K_0)) + B(o, \sqrt{d} \cdot a)\right) \\ &\leq 2 \left[\mathcal{H}^d\left(B(x, R) \cap V_x(K_0) + B(o, \sqrt{d} \cdot a)\right) - \mathcal{H}^d(B(x, R) \cap V_x(K_0)) \right] \\ &\leq 2 \left[\mathcal{H}^d\left(B(x, R) \cap V_x(K_0) + \frac{\sqrt{d} \cdot a}{r_x \wedge R} \cdot (B(x, R) \cap V_x(K_0))\right) - \mathcal{H}^d(B(x, R) \cap V_x(K_0)) \right] \\ &= \left[\left(1 + \frac{\sqrt{d} \cdot a}{r_x \wedge R}\right)^d - 1 \right] \mathcal{H}^d(B(x, R) \cap V_x(K_0)) \\ &\leq c_1(d) \cdot \max \left\{ \frac{a}{\mathbf{N}(K_0) \wedge R}, \left(\frac{a}{\mathbf{N}(K_0) \wedge R}\right)^d \right\} \mathcal{H}^d(B(x, R) \cap V_x(K_0)), \end{aligned}$$

and hence

$$\begin{aligned} &\mathcal{H}^d\left(\partial(B(x, R) \cap V_x(K_0)) + B(o, \sqrt{d} \cdot a)\right) \\ &\leq c_2(d, \rho, R) \cdot \max \left\{ \frac{a}{\mathbf{N}(K_0)}, \left(\frac{a}{\mathbf{N}(K_0)}\right)^d \right\} \mathcal{H}^d(B(x, R) \cap V_x(K_0)), \end{aligned} \quad (4.9)$$

where we use that $\mathbf{N}(K_0) \leq 2\rho$ if $R < \mathbf{N}(K_0)$. If $R \geq \mathbf{N}(K_0)$, then we can choose $c_2(d, \rho, R) = c_1(d)$. The sum of the volumes $\mathcal{H}^d(B(x, R) \cap V_x(K_0))$ over $x \in K_0$ is bounded from above by $\kappa_d(\rho + R)^d$. Combination of (4.7), (4.8), and (4.9) finally yields

$$\begin{aligned} &|\widehat{\mathcal{V}}_R^{r,s}(K_0, a) - \mathcal{V}_R^{r,s}(K_0)| \\ &\leq d\rho^r R^{s-1} (2\rho + R)^d \cdot \left(s \cdot a + R \cdot c_2(d, \rho, R) \cdot \max \left\{ \frac{a}{\mathbf{N}(K_0)}, \left(\frac{a}{\mathbf{N}(K_0)}\right)^d \right\} \right), \end{aligned}$$

which implies the required bound, since $\mathbf{N}(K_0) \leq 2\rho$. \square

From the comments after (4.4) and the proof of Theorem 4.3, which yields more explicit information about the constants involved, we get the following consequence.

Corollary 4.4. *Let $K \subset \mathbb{R}^d$ be a compact set, and let $r, s \in \mathbb{N}_0$. Let $\rho > 0$ be such that $K \subseteq B(o, \rho)$. If $K_0 \subseteq B(o, \rho)$ is a finite set, $R \leq R_0$, and $0 < a \leq \mathbf{N}(K_0) \wedge R$, then almost surely*

$$|\widehat{\mathcal{V}}_R^{r,s}(K_0, a) - \mathcal{V}_R^{r,s}(K)| \leq C'''(d, R_0, \rho, r, s) \left(d_H(K, K_0)^{\frac{1}{2}} + \frac{a}{\mathbf{N}(K_0) \wedge R} \right),$$

where $C'''(d, R_0, \rho, r, s) > 0$ is a constant depending only on d, R_0, ρ, r, s , and $d_H(K, K_0)^{\frac{1}{2}}$ can be replaced by $d_H(K, K_0)$ if $r = s = 0$.

Combination of Corollary 4.1 and Corollary 4.4 finally yields the next result. It serves as a theoretical foundation for the approximation of surface tensors of finite unions of sets with positive reach via Corollary 4.1. We remark that for any nonempty compact set $K \subset \mathbb{R}^d$, the finite set

$$K(n) := \left\{ (\sqrt{dn})^{-1} \cdot z : z \in \mathbb{Z}^d, \text{dist}(K, (\sqrt{dn})^{-1} \cdot z) \leq \frac{1}{n} \right\} \quad (4.10)$$

satisfies $d_H(K(n), K) \leq \frac{1}{n}$.

Theorem 4.5. *Let $K \subset \mathbb{R}^d$ be a finite union of compact sets with positive reach, and let $r \in \mathbb{N}_0$, $s \in \mathbb{N}$. Let $\rho > 0$ be such that $K \subseteq B(o, \rho)$. If $(\varepsilon_n)_{n \in \mathbb{N}}$ satisfies $\varepsilon_n \rightarrow 0_+$ as $n \rightarrow \infty$, then there exist sequences $(K_0(n))_{n \in \mathbb{N}}$ of finite subsets of \mathbb{R}^d with $K_0(n) \rightarrow K$ as $n \rightarrow \infty$ and $(a_n)_{n \in \mathbb{N}}$ of real numbers such that, almost surely,*

$$\lim_{n \rightarrow \infty} \frac{\widehat{\mathcal{V}}_{\varepsilon_n}^{r,s}(K_0(n), a_n)}{\varepsilon_n^{1+s}} = r!s!\kappa_{s+1}\Phi_{d-1}^{r,s}(K)$$

and

$$\lim_{n \rightarrow \infty} \frac{1}{\varepsilon_n} \left(\widehat{\mathcal{V}}_{\varepsilon_n}^{r,0}(K_0(n), a_n) - \widehat{\mathcal{V}}_{\varepsilon_n^2}^{r,0}(K_0(n), a_n) \right) = r!2\Phi_{d-1}^{r,0}(K).$$

Proof. We consider only the case $s = 0$, the argument for $s \in \mathbb{N}$ is similar (but easier). By Corollary 4.1, for $n \in \mathbb{N}$ there is some $\varepsilon(n) > 0$ such that

$$\left| \frac{1}{\varepsilon} \left(\mathcal{V}_{\varepsilon}^{r,0}(K) - \mathcal{V}_{\varepsilon^2}^{r,0}(K) \right) - r!2\Phi_{d-1}^{r,0}(K) \right| \leq \frac{1}{2n} \quad \text{if } 0 < \varepsilon \leq \varepsilon(n). \quad (4.11)$$

where $\varepsilon(n+1) < \varepsilon(n) \leq \varepsilon(1) \leq 1$ for $n \in \mathbb{N}$ and $\varepsilon(n) \rightarrow 0_+$ as $n \rightarrow \infty$.

We can assume that $\varepsilon_m \leq \varepsilon(1)$ for $m \in \mathbb{N}$. For $m \in \mathbb{N}$ there is a unique $n \in \mathbb{N}$ such that $\varepsilon_m \in (\varepsilon(n+1), \varepsilon(n)]$. By the remarks preceding Theorem 4.5, there is a finite set $K_0(m) \subset \mathbb{R}^d$ such that

$$d_H(K, K_0(m)) \leq (C''(d, \varepsilon(1), \rho, r, 0)8n)^{-2} \cdot \varepsilon_m^2. \quad (4.12)$$

Moreover, we choose

$$a_m \leq \frac{\mathbf{N}(K_0(m)) \wedge \varepsilon_m^2}{C''(d, \varepsilon(1), \rho, r, 0)8n} \cdot \varepsilon_m, \quad (4.13)$$

where we can assume that $C''(d, \varepsilon(1), \rho, r, 0)4n \geq 1$, so that

$$0 < a_m \leq \mathbf{N}(K_0(m)) \wedge \varepsilon_m^2 \leq \mathbf{N}(K_0(m)) \wedge \varepsilon_m \leq 1.$$

Corollary 4.4, (4.12) and (4.13) then yield almost surely

$$\left| \widehat{\mathcal{V}}_{\varepsilon_m}^{r,0}(K_0(m), a_m) - \mathcal{V}_{\varepsilon_m}^{r,0}(K) \right| \leq \frac{\varepsilon_m}{4n}, \quad \left| \widehat{\mathcal{V}}_{\varepsilon_m^2}^{r,0}(K_0(m), a_m) - \mathcal{V}_{\varepsilon_m^2}^{r,0}(K) \right| \leq \frac{\varepsilon_m}{4n},$$

hence

$$\left| \frac{1}{\varepsilon_m} \left(\widehat{\mathcal{V}}_{\varepsilon_m}^{r,0}(K_0(m), a_m) - \widehat{\mathcal{V}}_{\varepsilon_m^2}^{r,0}(K_0(m), a_m) \right) - \frac{1}{\varepsilon_m} \left(\mathcal{V}_{\varepsilon_m}^{r,0}(K) - \mathcal{V}_{\varepsilon_m^2}^{r,0}(K) \right) \right| \leq \frac{1}{2n}. \quad (4.14)$$

Combining (4.11) with $\varepsilon = \varepsilon_m$ and (4.14), we arrive at

$$\left| \frac{1}{\varepsilon_m} \left(\widehat{\mathcal{V}}_{\varepsilon_m}^{r,0}(K_0(m), a_m) - \widehat{\mathcal{V}}_{\varepsilon_m^2}^{r,0}(K_0(m), a_m) \right) - r!2\Phi_{d-1}^{r,0}(K) \right| \leq \frac{1}{n},$$

which implies the assertion. \square

Using the estimator from (4.6), Corollary 4.1 can in principle be applied directly to estimate the tensors $\Phi_{d-1}^{r,s}(K)$ from Corollary 4.1 by choosing a very small value for R , whenever K is a finite union of compact sets with positive reach and $s \geq 1$. We tested the performance for a rectangle $[-\frac{3}{2}, \frac{3}{2}] \times [-\frac{5}{2}, \frac{5}{2}]$ (see Example 4.9), a spherical shell with inner radius 1 and outer radius 2 (see Example 4.10), and for a rectangle from which a smaller (open) rectangle has been removed (see Example 4.11). The generated finite test data are obtained by intersecting these objects with a grid. The simulated estimates can be found in Table 2. To achieve good results, however, we needed an a that is significantly smaller than R , which itself must already be small. Since a small value of a considerably slows down the computation of the estimator from (4.6), this is a substantial disadvantage in practice. Therefore, for estimating the tensors from Corollary 4.1 we propose to use the alternative approach via a least squares problem, whenever it is applicable. For example, a single rendition (i.e., a run of the algorithm that provides an estimate) for the spherical shell S in the simulations for Table 2 took about 21 minutes on a standard personal computer, whereas in the simulations from Table 5 with the approach via a least squares problem, all 25 renditions for the same spherical shell took only about 3 minutes on a standard personal computer. Note that two renditions differ in the grid (4.5) used, as randomness only comes into play here. Surprisingly, the alternative approach led to excellent results even in cases where we only have a heuristic justification (see Table 6 for Example 4.11). Finally, we point out that we observed that the second part of Theorem 4.5, namely the approach for $s = 0$, requires far too much runtime and memory capacity for practical applications. Since a must be significantly smaller than ε and ε^2 for the application of the Theorem, and ε itself should already be a very small value, a becomes too small (and thus the number of points in the lattice process too large) for practical use. However, for $r = s = 0$ this problem can be overcome, as the following remark demonstrates.

Remark 4.6. Let K be a finite union of compact sets with positive reach and $\text{tr}(T)$ the trace of a tensor $T \in \mathbb{T}^2(\mathbb{R}^d)$, that is, $\text{tr}(T) := \sum_{j=1}^d T(e_j, e_j)$. Then it is true that

$$\text{tr}(\Phi_{d-1}^{0,2}(K)) = \frac{1}{4\pi} \Phi_{d-1}^{0,0}(K),$$

where we used that $\text{tr}(u^2) = 1$ for $u \in \mathbb{S}^{d-1}$ and the linearity of the trace operator.

In the following, we explain the algorithm that we will focus on for the remainder of the paper. The algorithm is based on the idea from [21] (see Section 3.2 there) to estimate the Minkowski tensors of a set K with positive reach by first approximating K by a simpler set K_0 (for instance, K_0 could be a finite subset of K) and by solving a linear system $Ax = b$. The solution x of the system is the $(d+1)$ -dimensional vector containing the estimated Minkowski tensors $\hat{\Phi}_d^{r,s}(K_0), \dots, \hat{\Phi}_0^{r,s}(K_0)$, where $r, s \in \mathbb{N}_0$. The vector b contains the estimated Voronoi tensors $\hat{\mathcal{V}}_{R_0}^{r,s}(K_0), \dots, \hat{\mathcal{V}}_{R_d}^{r,s}(K_0)$, for $d+1$ different values $0 < R_0 < \dots < R_d$ of the radius, and the matrix A is a Vandermonde-type matrix. It is shown in [21] that the solution of this system yields the exact values of the Minkowski tensors whenever the exact values of the Voronoi tensors are plugged in and R_d is smaller than the reach of K . Since inverting a matrix is numerically not stable, we replace the matrix inversion by a least squares problem, which allows us to use more than only $d+1$ equations. However, the basic idea of our algorithm remains to estimate the Minkowski tensors of K via the Voronoi tensors of a finite set K_0 . Here K_0 can be viewed as a finite approximation of a possibly infinite set K . In practice K_0 is usually considered to be a finite sample of points in K , while for generating test data one can intersect K with a grid.

Table 2: Results for the 2-dimensional rectangle $K = [-\frac{3}{2}, \frac{3}{2}] \times [-\frac{5}{2}, \frac{5}{2}]$, the spherical shell S with inner radius 1 and outer radius 2 (see Example 4.10) and $R_{a,b}$ from Example 4.11 with $a = (1, 2)^\top$, $b = (3, 5)^\top$ by using the estimator from (4.6) and the result from Corollary 4.1. We intersected $K, S, R_{a,b}$ with a grid of resolution 0.0005 and choose $R = \varepsilon = 0.05$ and $a = 0.0005$. We took the average of 25 renditions. All values are rounded to the fourth significant digit.

Tensors	Values	Estimates	Tensors	Values	Estimates
$(\Phi_1^{0,2}(K))_{1,1}$	0.3979	0.4029	$(\Phi_1^{0,2}(K))_{1,2}$	0	$-1.192 \cdot 10^{-4}$
$(\Phi_1^{0,2}(K))_{2,2}$	0.2387	0.2438	$(\Phi_1^{0,2}(S))_{1,1}$	0.3754	0.3754
$(\Phi_1^{0,2}(S))_{1,2}$	0	$1.286 \cdot 10^{-4}$	$(\Phi_1^{0,2}(S))_{2,2}$	0.3755	0.3757
$(\Phi_1^{0,2}(R_{a,b}))_{1,1}$	0.5560	0.5564	$(\Phi_1^{0,2}(R_{a,b}))_{1,2}$	0	$-1.287 \cdot 10^{-4}$
$(\Phi_1^{0,2}(R_{a,b}))_{2,2}$	0.3173	0.3178			

Now fix $a > 0$, an integer $n \geq d + 1$, and $0 < R_1 < \dots < R_n$. One of the key ideas of the algorithm is to replace the matrix inversion from [21] by a linear least squares problem. Extending the linear system from [21, (6)], we define the estimators $\widehat{\Phi}_j^{r,s}(K_0, a, R)$, $i \in \{0, \dots, d\}$, as the solution of the linear least squares problem

$$\widehat{\mathcal{V}}_{R_i}^{r,s}(K_0, a) = \sum_{k=0}^d r!s!\kappa_{k+s}R_i^{k+s}\widehat{\Phi}_{d-k}^{r,s}(K_0, a, R), \quad i \in \{1, \dots, n\}, \quad (4.15)$$

where $R := (R_1, \dots, R_n)$. Recall that κ_n denotes the volume of an n -dimensional unit ball. Moreover, a symmetric tensor $T \in \mathbb{T}^{r+s}(\mathbb{R}^d)$ of rank $r + s$ is determined by the values $T(e_{i_1}, \dots, e_{i_{r+s}})$ for $1 \leq i_1 \leq \dots \leq i_{r+s} \leq d$ (see (2.1)). The algorithm computes the tensors $\widehat{\Phi}_j^{r,s}(K_0, a, R)$, $i \in \{0, \dots, d\}$, by solving the least squares problem from (4.15) for each choice of $1 \leq i_1 \leq \dots \leq i_{r+s} \leq d$, using standard methods. The following lemma is well known (see [9, Theorems 1.1.5 and 1.1.6] or [20, Theorem 9]).

Lemma 4.7. *Let $s \in \mathbb{N}_0$ and $n \geq d + 1$. Let $x_1, y_1, \dots, x_n, y_n \in \mathbb{R}$, $c_0, \dots, c_d \in \mathbb{R} \setminus \{0\}$ and*

$$X := \left(c_j x_i^{s+j} \right)_{\substack{i=1, \dots, n \\ j=0, \dots, d}} \in \mathbb{R}^{n \times (d+1)}, \quad y := (y_1, \dots, y_n)^\top \in \mathbb{R}^n. \quad (4.16)$$

If $x_i \neq x_j$ for $i \neq j$, then X has rank $d + 1$ and $\mathbf{a} = (X^\top X)^{-1} X^\top y \in \mathbb{R}^{d+1}$ is the unique vector satisfying

$$\mathbf{a} = \arg \min \left\{ \sum_{i=1}^n (b_0 c_0 x_i^s + \dots + b_d c_d x_i^{s+d} - y_i)^2 \mid (b_0, \dots, b_d)^\top \in \mathbb{R}^{d+1} \right\}.$$

Remark 4.8. If $s \geq 1$, then we can also consider the matrix in $\mathbb{R}^{n \times d}$ with $n \geq d$ obtained from X by deleting the first column and setting $b_0 = 0$, which corresponds to the definition $\Phi_d^{r,s} = 0$ if $s \neq 0$.

As a consequence of Lemma 4.7 the least squares problem from (4.15) is continuous, that is whenever the input vector converges to some vector $b \in \mathbb{R}^n$, the solution will converge to the

solution of the least squares problem with input b . In particular, if K is a set with positive reach and R_n is less than the reach of K , then the tensors $\widehat{\Phi}_j^{r,s}(K_0, a, R)$ from (4.15) converge to $\Phi_j^{r,s}(K)$ as $\widehat{\mathcal{V}}_R^{r,s}(K_0, a)$ converges to $\mathcal{V}_R^{r,s}(K)$, for which Theorem 4.3 provides sufficient conditions. Note that the approximating tensors $\widehat{\Phi}_j^{r,s}(K_0, a, R)$ depend on the choice of the fixed radii $0 < R_1 < \dots < R_n$, but the Minkowski tensors $\Phi_j^{r,s}(K)$ will be independent of the radii (as they should be) as long as K has reach greater than R_n . We would like to point out that although the solution to the least squares problem from Lemma 4.7 involves a matrix inversion, the algorithm for solving the problem does not compute an inverse matrix. Lemma 4.7 merely serves to show that the solution is continuous with respect to the input. In our situation we apply Lemma 4.7 for each choice of $1 \leq i_1 \leq \dots \leq i_{r+s} \leq d$ to

$$x_i = R_i, \quad c_i = r!s!\kappa_{i+s}, \quad y_i = \widehat{\mathcal{V}}_{R_i}^{r,s}(K_0, a)(e_{i_1}, \dots, e_{i_{r+s}}),$$

to obtain $\widehat{\Phi}_{d-j}^{r,s}(K_0, a, R)(e_{i_1}, \dots, e_{i_{r+s}})$ for $j \in \{0, \dots, d\}$. So there are two main tasks involved in the algorithm: To estimate the Voronoi tensors of K_0 with respect to the n values R_1, \dots, R_n by the estimator in (4.6) and then to solve the system (4.15). Therefore the only randomness involved in the algorithm is contained in the random grid η .

We now explain the role of the relevant quantities. As an input the algorithm takes a finite set K_0 , the rank parameters $r, s \in \mathbb{N}_0$ of the Minkowski tensors, the number $n \geq d + 1$ of equations as well as the maximal radius R_n . The smallest radius R_1 used is the average nearest neighbor distance in K_0 , that is

$$av(K_0) := \frac{1}{|K_0|} \sum_{x \in K_0} \min\{\|x - z\| : z \in K_0 \setminus \{x\}\},$$

where $|K_0|$ denotes the cardinality of K_0 . The other radii are chosen equidistantly between R_1 and R_n . Therefore we have the additional condition that R_n has to be greater than $av(K_0)$, and we recommend to choose R_n to be at least $(d + 1) \cdot av(K_0)$. The resolution a of the random grid η is also chosen as $av(K_0)$.

It is also possible to provide the algorithm with an observation window

$$W = \prod_{i=1}^d [a_i, b_i], \quad a_i < b_i \text{ for } i \in \{1, \dots, d\},$$

instead of R_n . In this case the algorithm computes the distance of the data from the boundary of the observation window in each direction and chooses the minimum of these values for R_n . By the distance of K_0 from the boundary of W in some direction $s \cdot e_j$, where $s \in \{-1, 1\}$ and e_j denotes the j -th standard unit vector, we mean

$$\begin{aligned} \min\{b_j - x_j : x = (x_1, \dots, x_d)^\top \in K_0\}, & \quad s = 1, \\ \min\{x_j - a_j : x = (x_1, \dots, x_d)^\top \in K_0\}, & \quad s = -1. \end{aligned}$$

The output of the algorithm consists of a list containing the $d + 1$ estimated Minkowski tensors $\widehat{\Phi}_d^{r,s}(K_0, a, R), \dots, \widehat{\Phi}_0^{r,s}(K_0, a, R)$ (in this order), where a tensor is given as a dictionary whose keys are the indices of the individual values. Note that the tensors are symmetric and therefore the algorithm does not estimate all the values since some of them are redundant. For a tuple of indices $(i_1, \dots, i_{r+s}) \in \{1, \dots, d\}^{r+s}$ with $i_1 \leq \dots \leq i_{r+s}$ the algorithm estimates the value of the tensor corresponding to these indices, but not those corresponding to permutations of the tuple since they are the same. Table 3 shows a small summary of the input of the algorithm.

Table 3: Input parameters of the algorithm

K_0	finite input data
r, s	rank parameters of the Minkowski tensors
n	number of equations considered ($n \geq d + 1$)
R_n	maximal radius considered (we recommend $R_n \geq (d + 1)R_1$)
W	observation window containing K_0 (optional instead of R_n)

4.2 Implementation

The algorithm is implemented in Python, and the code is available via an open-source package [47]. One can apply the algorithm by using the Python functions `Voromink` and `Vorosurf` in the file `VorominkEstimation.py`. Details can be found in the description of the code, which can also be found in [47]. Closely following the above described estimation of the Minkowski tensors, the user chooses some rank parameters $r, s \in \mathbb{N}_0$. Then the algorithm will return estimators of the $d + 1$ Minkowski tensors $\Phi_0^{r,s}(K), \dots, \Phi_d^{r,s}(K)$, based on the input data K_0 and the dimension d , for a (in general) unknown set K . The algorithm also offers the option to rotate the random grid η on which the algorithm is based. This option is useful for test data that lies somehow parallel to the axis spanned by the standard vectors. For real data this rotation should, in general, not be necessary and can be skipped to further reduce the run time (especially in high dimensions).

We found the run times of our code to be convenient for practically relevant examples. For example, a single rendition of the simulations for a two-dimensional rectangle (results can be found in Appendix A), containing about 150,000 points, took an average of 30 seconds. In this case, the algorithm was applied for 5 different rank parameter tuples (r, s) (all possible combinations with $r + s \leq 2$), and for each tuple, 50 runs were performed (resulting in a total of 250 runs and a computation time of 1.5 hours). Computation time scales with the number of points of the grid process η . Therefore the time increases highly with the dimension d and with a refinement of the resolution of the grid process which is taken as the average nearest neighbor distance $av(K_0)$ of the input data K_0 . According to Theorem 4.3, it would theoretically be better to choose the grid resolution even smaller than $av(K_0)$. However, in our simulations, we found that this did not significantly improve the results but considerably increased the runtime.

4.3 Choice of parameters

The choices of the parameters n, R_n has a big influence on the results of the algorithm. Therefore we share the experience we made while working with the algorithm. For the parameter n we obtained better results for higher values. In principle one can choose n as big as possible, but the distances $R_{i+1} - R_i$ between the values of consecutive radii should not be smaller than the average nearest neighbor distance in the test data. We often used the value $n = 50$.

The choice of the parameter R_n is much more intricate. The theory requires the value of R_n to be smaller than the reach of the original set K that is represented by the data K_0 . In practice this value is usually unknown. If the original set is supposed to be convex, R_n could in principle be arbitrarily big. In the general case one should choose this parameter depending on an assessment of the data. It is important that R_n is not too small. We recommend it to be at

least $d+1$ times the average nearest neighbor distance $av(K_0)$ in the test data K_0 , but from our experiences this value sometimes needs to be increased further. For more advanced applications and requirements, Bayesian optimization can be a helpful tool for obtaining the best possible parameters.

4.4 Convex test cases

In this section we present some simulation results showing how the algorithm works for specific simulated test data. We tested the algorithm for rectangles in dimension $d \in \{2, 3\}$ as well as for a rectangle in dimension 2 with rounded vertices. To generate the data we fixed a grid $a \cdot \mathbb{Z}^d$ and intersected it with the rectangle. Table 4 shows formulas for the Minkowski tensors with rank at most 2 of a rectangle of the form $[-\frac{a_1}{2}, \frac{a_1}{2}] \times [-\frac{a_2}{2}, \frac{a_2}{2}] \subset \mathbb{R}^2$. These formulas can be obtained by the following simplification of the Minkowski tensors of polytopes. For any polytope $P \subset \mathbb{R}^d$ we have

$$\begin{aligned} \Phi_k^{r,s}(P) &= \frac{1}{r!s!} \frac{1}{\omega_{d-k+s}} \sum_{F \in \mathcal{F}_k(P)} \int_F \int_{N(P,F) \cap \mathbb{S}^{d-1}} x^r u^s \mathcal{H}^{d-k-1}(du) \mathcal{H}^k(dx), \quad k < d, \\ \Phi_d^{r,0}(P) &= \frac{1}{r!} \int_P x^r dx, \quad \Phi_d^{r,s}(P) = 0, \quad s > 0, \end{aligned}$$

where $\mathcal{F}_k(P)$ is the set of the k -dimensional faces of the polytope P and $N(P, F)$ is the normal cone of P with respect to the face F . Recall that \mathcal{H}^k denotes the k -dimensional Hausdorff measure and ω_k is the surface area of the unit sphere \mathbb{S}^{k-1} in \mathbb{R}^k .

Example 4.9. Let $R = [-\frac{a_1}{2}, \frac{a_1}{2}] \times [-\frac{a_2}{2}, \frac{a_2}{2}] \subset \mathbb{R}^2$ be a two-dimensional rectangle with side lengths a_1 and a_2 . Then the above formula yields for $r = 2, s = 0, k = 1$ that

$$\Phi_1^{2,0}(R) = \frac{1}{4} \sum_{F \in \mathcal{F}_1(R)} \int_F x^2 \mathcal{H}^1(dx).$$

Using $x^2 = x_1^2 e_1^2 + 2x_1 x_2 e_1 e_2 + x_2^2 e_2^2$, for an edge of the form $F = [-\frac{a_1}{2}, \frac{a_1}{2}] \times \{\pm \frac{a_2}{2}\}$ we obtain

$$\int_F x^2 \mathcal{H}^1(dx) = \int_{-\frac{a_1}{2}}^{\frac{a_1}{2}} y^2 e_1^2 \pm y a_2 e_1 e_2 + \frac{a_2^2}{4} e_2^2 dy = \frac{a_1^3}{12} e_1^2 + \frac{a_1 a_2^2}{4} e_2^2.$$

Therefore the summation over all the edges of R yields

$$\Phi_1^{2,0}(R) = \frac{1}{24} ((a_1^3 + 3a_1^2 a_2) e_1^2 + (3a_1 a_2^2 + a_2^3) e_2^2).$$

For $r = s = k = 1$ we obtain

$$\Phi_1^{1,1}(R) = \frac{1}{2\pi} \sum_{F \in \mathcal{F}_1(R)} \int_F \int_{N(R,F) \cap \mathbb{S}^1} x u \mathcal{H}^0(du) \mathcal{H}^1(dx).$$

As before we start by computing the integral for an edge of the form $F = [-\frac{a_1}{2}, \frac{a_1}{2}] \times \{\pm \frac{a_2}{2}\}$. The normal cone of this set intersected with the unit sphere is given by $\{\pm e_2\}$. Since the tensor $x e_2$ can be written as $x_1 e_1 e_2 + x_2 e_2^2$, we obtain

$$\int_F \int_{N(R,F) \cap \mathbb{S}^1} x u \mathcal{H}^0(du) \mathcal{H}^1(dx) = \pm \int_F x e_2 \mathcal{H}^1(dx) = \pm \int_{-\frac{a_1}{2}}^{\frac{a_1}{2}} y e_1 e_2 \pm \frac{a_2}{2} e_2^2 dy = \frac{a_1 a_2}{2} e_2^2.$$

Table 4: Formulas for the Minkowski tensors with rank at most 2 of a rectangle of the form $[-\frac{a_1}{2}, \frac{a_1}{2}] \times [-\frac{a_2}{2}, \frac{a_2}{2}] \subset \mathbb{R}^2$, where the values of $\Phi_k^{1,0}$, $\Phi_k^{0,1}$ vanish for all $k \in \{0, 1, 2\}$.

Tensor	Formula	Tensor	Formula	Tensor	Formula
$\Phi_0^{0,0}$	1	$\Phi_1^{0,0}$	$a_1 + a_2$	$\Phi_2^{0,0}$	$a_1 \cdot a_2$
$\Phi_0^{0,2}$	$\frac{1}{4\pi} (e_1^2 + e_2^2)$	$\Phi_1^{0,2}$	$\frac{1}{4\pi} (a_2 e_1^2 + a_1 e_2^2)$	$\Phi_2^{0,2}$	0
$\Phi_0^{2,0}$	$\frac{1}{8} (a_1^2 e_1^2 + a_2^2 e_2^2)$	$\Phi_1^{2,0}$	$\frac{1}{24} \sum_{i=1}^2 (a_i^3 + 3a_i^2 a_j) e_i^2$	$\Phi_2^{2,0}$	$\frac{1}{24} (a_1^3 a_2 e_1^2 + a_2^3 a_1 e_2^2)$
$\Phi_0^{1,1}$	$\frac{1}{2\pi} (a_1 e_1^2 + a_2 e_2^2)$	$\Phi_1^{1,1}$	$\frac{a_1 a_2}{2\pi} (e_1^2 + e_2^2)$	$\Phi_2^{1,1}$	0

After taking the summation over all edges, we get

$$\Phi_1^{1,1}(R) = \frac{a_1 a_2}{2\pi} (e_1^2 + e_2^2) = \frac{a_1 a_2}{2\pi} Q.$$

The results of the algorithm for a two-dimensional rectangle can be found in Appendix A and are very close to the exact values. We also tested a 3-dimensional rectangle in the same way and obtained very good results. Further we considered a 2-dimensional rectangle with “rounded corners” and the results again were very close to the exact values (relative deviations of less than 1% for rectangles of varying sizes with up to 1.3 million points). The detailed results, along with those for a 3-dimensional rectangle, where we once again achieved very good outcomes, can be found in Appendix A.

4.5 Nonconvex test cases

If $A \subset \mathbb{R}^d$ is a set of positive reach, the boundary ∂A of A is of class C^2 , and A has a unique exterior unit outer normal vector $\nu(A, x)$ at each $x \in \partial A$, then

$$\Lambda_m(A, \cdot) = \frac{1}{\omega_{d-m}} \int_{\partial A} \mathbb{1}\{(x, \nu(A, x)) \in \cdot\} \sum_{|I|=d-1-m} \prod_{i \in I} k_i(A, x) \mathcal{H}^{d-1}(dx),$$

where $k_1(A, x), \dots, k_{d-1}(A, x) \in \mathbb{R}$ are the principal curvatures of A at $x \in \partial A$ and the summation extends over all subsets $I \subset \{1, \dots, d-1\}$ of cardinality $|I| = d-1-m$ (if $m = d-1$ the empty product is interpreted as 1). Thus we obtain, for $k \in \{0, \dots, d-1\}$,

$$\Phi_k^{r,s}(A) = \frac{1}{r!s!\omega_{d-k+s}} \int_{\partial A} x^r \nu(A, x)^s \sum_{|I|=d-1-m} \prod_{i \in I} k_i(A, x) \mathcal{H}^{d-1}(dx).$$

Example 4.10. Let $A = \{x \in \mathbb{R}^d : \rho_1 \leq \|x\| \leq \rho_2\}$ denote a spherical shell with inner radius ρ_1 and outer radius ρ_2 , where $0 \leq \rho_1 < \rho_2 < \infty$. Observe that the reach of A is ρ_1 whenever $\rho_1 > 0$ (if $\rho_1 = 0$, then A is a Euclidean ball with radius ρ_2). Since the principal curvatures of A at $x \in \partial A$ are equal to ρ_2^{-1} , if $\|x\| = \rho_2$, and equal to $-\rho_1^{-1}$, if $\|x\| = \rho_1 > 0$, we simply write

Table 5: Results for the 2-dimensional spherical shell with inner radius $\rho_1 = 1$ and outer radius $\rho_2 = 2$ intersected with a grid of resolution $a = 0.005$. The parameter choices were $n = 50$ and $R_n = 1.8$ (0.9 times the reach of the spherical shell). We took the average of 25 renditions. All values are rounded to the fourth significant digit.

Tensors	Values	Algorithm	Tensors	Values	Algorithm
$\Phi_0^{0,0}$	0	$-9.621 \cdot 10^{-3}$	$\Phi_1^{0,0}$	9.4248	9.4441
$\Phi_2^{0,0}$	9.4248	9.4018	$(\Phi_1^{0,2})_{1,1}$	0.3749	0.3749
$(\Phi_1^{0,2})_{1,2}$	0	$1.432 \cdot 10^{-4}$	$(\Phi_1^{0,2})_{2,2}$	0.3749	0.3748
$(\Phi_1^{1,1})_{1,1}$	1.5	1.495	$(\Phi_1^{1,1})_{1,2}$	0	$-2.574 \cdot 10^{-3}$
$(\Phi_1^{1,1})_{2,2}$	1.5	1.492			

$k(A, x)$ for these principal curvatures and get

$$\begin{aligned}
\Phi_k^{r,s}(A) &= \frac{\binom{d-1}{k}}{r!s!\omega_{d-k+s}} \int_{\partial A} x^r \nu(A, x)^s k(A, x)^{d-1-k} \mathcal{H}^{d-1}(dx) \\
&= \frac{\binom{d-1}{k}}{r!s!\omega_{d-k+s}} \int_{\mathbb{S}^{d-1}} \left((\rho_2 u)^r u^s \rho_2^{k+1-d} \rho_2^{d-1} + (\rho_1 u)^r (-u)^s (-\rho_1)^{k+1-d} \rho_1^{d-1} \right) \mathcal{H}^{d-1}(du) \\
&= \frac{\binom{d-1}{k}}{r!s!\omega_{d-k+s}} \left(\rho_2^{r+k} + (-1)^{s+d-1-k} \rho_1^{r+k} \right) \int_{\mathbb{S}^{d-1}} u^{r+s} \mathcal{H}^{d-1}(du) \\
&= \mathbf{1}\{r+s \text{ even}\} \frac{\binom{d-1}{k} 2\omega_{d+r+s}}{r!s!\omega_{d-k+s}\omega_{r+s+1}} \left(\rho_2^{r+k} + (-1)^{s+d-1-k} \rho_1^{r+k} \right) Q^{\frac{r+s}{2}},
\end{aligned}$$

where the transformation formula and [27, Lemma 7] have been used to determine the integral.

If $k = d - 1$, this specializes to

$$\Phi_{d-1}^{r,s}(A) = \mathbf{1}\{r+s \text{ even}\} \frac{2\omega_{d+r+s}}{r!s!\omega_{s+1}\omega_{r+s+1}} \left(\rho_2^{r+d-1} + (-1)^s \rho_1^{r+d-1} \right) Q^{\frac{r+s}{2}},$$

and if $k = d - 1$ and $r = 0$, we obtain

$$\Phi_{d-1}^{0,s}(A) = \mathbf{1}\{s \text{ even}\} \frac{2\omega_{d+s}}{s!\omega_{s+1}^2} \left(\rho_1^{d-1} + \rho_2^{d-1} \right) Q^{\frac{s}{2}}.$$

Table 5 shows simulation results for the 2-dimensional spherical shell with inner radius $\rho_1 = 1$ and outer radius $\rho_2 = 2$.

Example 4.11. Let $R_a = [-\frac{a_1}{2}, \frac{a_1}{2}] \times [-\frac{a_2}{2}, \frac{a_2}{2}] \subset \mathbb{R}^2$ be a two-dimensional rectangle with side lengths a_1 and a_2 and $a = (a_1, a_2)^\top \in \mathbb{R}^2$. For $0 < a_1 < b_1$ and $0 < a_2 < b_2$ we consider $R_{a,b} := R_b \setminus R_a^\circ$, i.e., the interior of the rectangle R_a is removed from the enclosing rectangle R_b . The set $R_{a,b}$ does not have positive reach, but it is a polyconvex set and in particular a finite union of compact sets with positive reach. The surface tensors $\Phi_1^{r,s}(R_{a,b})$ can be expressed in terms of the surfaces tensors of R_a and R_b by

$$\Phi_1^{r,s}(R_{a,b}) = \Phi_1^{r,s}(R_b) + (-1)^s \Phi_1^{r,s}(R_a),$$

where $r, s \in \mathbb{N}_0$; see Table 4 for explicit formulas. Table 6 shows simulation results for $R_{a,b}$ with $a = (1, 2)^\top$, $b = (3, 5)^\top$.

Table 6: Results for $R_{a,b}$ with $a = (1, 2)^\top$, $b = (3, 5)^\top$ intersected with a grid of resolution $a = 0.01$. The parameter choices were $n = 50$ and $R_n = 0.45$ ($0.9 \cdot 0.5$ times the length of the smaller side of R_a). We took the average of 25 renditions. All values are rounded to the fourth significant digit.

Tensors	Values	Algorithm	Tensors	Values	Algorithm
$\Phi_0^{0,0}$	0	-0.2837	$\Phi_1^{0,0}$	11	11.01
$\Phi_2^{0,0}$	13	13.00	$(\Phi_1^{0,2})_{1,1}$	0.5570	0.5477
$(\Phi_1^{0,2})_{1,2}$	0	$-1.528 \cdot 10^{-4}$	$(\Phi_1^{0,2})_{2,2}$	0.3183	0.3110
$(\Phi_1^{1,1})_{1,1}$	2.069	2.073	$(\Phi_1^{1,1})_{1,2}$	0	$2.931 \cdot 10^{-3}$
$(\Phi_1^{1,1})_{2,2}$	2.069	2.073			

5 Isotropic random polytopes

Next, we apply our algorithm to a common model of random convex polytopes. In Section 5.1 we first show how the expected value of the Minkowski tensors $\Phi_k^{0,s}(Z)$ for an isotropic random polytope Z can be expressed in terms of the metric tensor Q and the expected value of the intrinsic volume $V_k(Z)$. From this relation we then derive explicit formulas for beta-polytopes, a class of isotropic random polytopes that has proved to be useful in stochastic geometry (see, e.g., [32]). In Section 5.2, the exact evaluations of the resulting formulas are compared to the results of a simulation study based on our algorithm.

5.1 Exact expectations

In this section, we focus on the case $r = 0$. A random polytope Z in \mathbb{R}^d is said to be isotropic if ρZ and Z have the same distribution for all $\rho \in SO(d)$.

Lemma 5.1. *Let Z be an isotropic random polytope in \mathbb{R}^d . Let $k \in \{0, \dots, d-1\}$. If $\mathbb{E}V_k(Z) < \infty$, then*

$$\mathbb{E}\Phi_k^{0,s}(Z) = \mathbf{1}\{s \text{ even}\} \frac{2\omega_{d+s}\omega_{d-k}}{s!\omega_d\omega_{s+1}\omega_{d-k+s}} \mathbb{E}V_k(Z) \cdot Q^{\frac{s}{2}};$$

in particular, the surface tensors are given by

$$\mathbb{E}\Phi_{d-1}^{0,s}(Z) = \mathbf{1}\{s \text{ even}\} \frac{4\omega_{d+s}}{s!\omega_d\omega_{s+1}^2} \mathbb{E}V_{d-1}(Z) \cdot Q^{\frac{s}{2}}, \quad (5.1)$$

Proof. Let $\rho \in SO(d)$. Since Z is isotropic, we deduce from the definition of $\Phi_k^{0,s}(Z)$ that

$$\begin{aligned} \mathbb{E}\Phi_k^{0,s}(Z) &= \frac{1}{s!\omega_{d-k+s}} \mathbb{E} \sum_{F \in \mathcal{F}_k(\rho Z)} V_k(F) \int_{N(\rho Z, F) \cap \mathbb{S}^{d-1}} u^s \mathcal{H}^{d-k-1}(du) \\ &= \frac{1}{s!\omega_{d-k+s}} \mathbb{E} \sum_{F \in \mathcal{F}_k(Z)} V_k(\rho F) \int_{\rho N(Z, F) \cap \mathbb{S}^{d-1}} u^s \mathcal{H}^{d-k-1}(du) \\ &= \frac{1}{s!\omega_{d-k+s}} \mathbb{E} \sum_{F \in \mathcal{F}_k(Z)} V_k(F) \int_{N(Z, F) \cap \mathbb{S}^{d-1}} (\rho v)^s \mathcal{H}^{d-k-1}(dv). \end{aligned} \quad (5.2)$$

Integration of (5.2) over all $\rho \in SO(d)$ with respect to the Haar probability measure ν on $SO(d)$ and Fubini's theorem yield

$$\mathbb{E}\Phi_k^{0,s}(Z) = \frac{1}{s!\omega_{d-k+s}} \mathbb{E} \sum_{F \in \mathcal{F}_k(Z)} V_k(F) \int_{N(Z,F) \cap \mathbb{S}^{d-1}} \int_{SO(d)} (\rho v)^s \nu(d\rho) \mathcal{H}^{d-k-1}(dv).$$

The application of Fubini's theorem (in particular, interchanging expectation and integration) is justified since $\mathbb{E}V_k(Z) < \infty$. From

$$\int_{SO(d)} (\rho v)^s \nu(d\rho) = \frac{1}{\omega_d} \int_{\mathbb{S}^{d-1}} w^s \mathcal{H}^{d-1}(dw) = \mathbb{1}\{s \text{ even}\} \frac{2\omega_{d+s}}{\omega_d \omega_{s+1}} Q^{\frac{s}{2}}$$

(see, e.g., [27, Lemma 7] and the reference given there) we deduce that

$$\begin{aligned} \mathbb{E}\Phi_k^{0,s}(Z) &= \mathbb{1}\{s \text{ even}\} \frac{2\omega_{d+s}}{s!\omega_d \omega_{s+1} \omega_{d-k+s}} Q^{\frac{s}{2}} \mathbb{E} \sum_{F \in \mathcal{F}_k(Z)} V_k(F) \mathcal{H}^{d-k-1}(N(Z,F) \cap \mathbb{S}^{d-1}) \\ &= \mathbb{1}\{s \text{ even}\} \frac{2\omega_{d+s} \omega_{d-k}}{s!\omega_d \omega_{s+1} \omega_{d-k+s}} \mathbb{E}V_k(Z) \cdot Q^{\frac{s}{2}}, \end{aligned}$$

which proves the assertion. \square

We consider the case where $Z = P_{\ell,d}^\beta$ is a beta-polytope with $\beta > -1$. To define this class of random polytopes, let

$$f_{d,\beta}(x) := c_{d,\beta} \mathbb{1}\{\|x\| < 1\} \left(1 - \|x\|^2\right)^\beta, \quad x \in \mathbb{R}^d,$$

with the normalizing constant

$$c_{d,\beta} := \frac{\Gamma\left(\frac{d}{2} + \beta + 1\right)}{\pi^{\frac{d}{2}} \Gamma(\beta + 1)}.$$

Hence $f_{d,\beta}$ is the density of a beta-distribution in \mathbb{R}^d .

Let X_1, \dots, X_ℓ be i.i.d. random points in \mathbb{R}^d whose common distribution function has Lebesgue density $f_{d,\beta}$. If $\ell \geq d + 1$, then

$$P_{\ell,d}^\beta := \text{conv}\{X_1, \dots, X_\ell\}$$

is called a beta-polytope (see [32]) in \mathbb{R}^d (with parameters β and ℓ). Since the density $f_{d,\beta}$ is rotation invariant, the distribution of X_1, \dots, X_ℓ is rotation invariant, and hence $P_{\ell,d}^\beta$ is an isotropic random polytope. It follows from [31, Cor. 2.4] that

$$\mathbb{E}V_{d-1}(P_{\ell,d}^\beta) = \frac{d(2\beta + d + 1)}{2^d \Gamma\left(\frac{d}{2}\right)} \binom{\ell}{d} \left(\frac{\Gamma\left(\beta + \frac{d+2}{2}\right)}{\Gamma\left(\beta + \frac{d+3}{2}\right)}\right)^d \int_{-1}^1 (1 - h^2)^{d\beta + \frac{(d-1)(d+2)}{2}} F_{1,\beta + \frac{d-1}{2}}(h)^{\ell-d} dh$$

with

$$F_{1,\beta + \frac{d-1}{2}}(h) := \frac{\Gamma\left(\beta + \frac{d+2}{2}\right)}{\sqrt{\pi} \Gamma\left(\beta + \frac{d+1}{2}\right)} \int_{-1}^h (1 - x^2)^{\beta + \frac{d-1}{2}} dx, \quad h \in [-1, 1].$$

This expectation can be rewritten in the form

$$\begin{aligned} \mathbb{E}V_{d-1}(P_{\ell,d}^\beta) &= \frac{d\pi^{\frac{d}{2}}}{(2\beta + d + 1)^{d-1} \Gamma\left(\frac{d}{2}\right)} \binom{\ell}{d} \left(\frac{\Gamma\left(\beta + \frac{d+2}{2}\right)}{\sqrt{\pi} \Gamma\left(\beta + \frac{d+1}{2}\right)}\right)^\ell \\ &\quad \times \int_{-1}^1 (1 - h^2)^{d\beta + \frac{d-1}{2}(d+2)} \left(\int_{-1}^h (1 - x^2)^{\beta + \frac{d-1}{2}} dx\right)^{\ell-d} dh. \end{aligned}$$

If $\beta = -\frac{1}{2}$, then

$$\mathbb{E}V_{d-1}(P_{\ell,d}^{-\frac{1}{2}}) = \frac{\pi^{\frac{d}{2}}}{d^{d-2}\Gamma(\frac{d}{2})} \binom{\ell}{d} \left(\frac{\Gamma(\frac{d+1}{2})}{\sqrt{\pi}\Gamma(\frac{d}{2})} \right)^\ell \int_{-1}^1 \sqrt{1-h^2}^{d^2-2} \left(\int_{-1}^h \sqrt{1-x^2}^{d-2} dx \right)^{\ell-d} dh.$$

For $d = 2$ and $\ell \geq 3$ this simplifies to

$$\mathbb{E}V_1(P_{\ell,2}^{-\frac{1}{2}}) = \pi \frac{\ell-1}{\ell+1}.$$

If $\beta = \frac{1}{2}$, then

$$\begin{aligned} \mathbb{E}V_{d-1}(P_{\ell,d}^{\frac{1}{2}}) &= \frac{d\pi^{\frac{d}{2}}}{(d+2)^{d-1}\Gamma(\frac{d}{2})} \binom{\ell}{d} \left(\frac{\Gamma(\frac{d+3}{2})}{\sqrt{\pi}\Gamma(\frac{d+2}{2})} \right)^\ell \\ &\quad \times \int_{-1}^1 \sqrt{1-h^2}^{d^2+2d-2} \left(\int_{-1}^h \sqrt{1-x^2}^d dx \right)^{\ell-d} dh. \end{aligned}$$

If $d = 2$, this simplifies to

$$\mathbb{E}V_1(P_{\ell,2}^{\frac{1}{2}}) = \pi \cdot \ell(\ell-1) \frac{9}{4^{\ell+1}} \int_{-1}^1 (1-h)^3 (1+h)^{2\ell-1} (2-h)^{\ell-2} dh.$$

Expansion of $(2-h)^{\ell-2} = (1+(1-h))^{\ell-2}$ and repeated partial integration yield

$$\mathbb{E}V_1(P_{\ell,2}^{\frac{1}{2}}) = \pi \cdot 9(\ell-1) \sum_{j=0}^{\ell-2} \frac{\binom{\ell-2}{j}}{\binom{2\ell+j+3}{j+3}} 2^j.$$

From (5.1) we have

$$\mathbb{E}\Phi_{d-1}^{0,s}(P_{\ell,d}^\beta) = \mathbf{1}\{s \text{ even}\} \frac{4\omega_{d+s}}{s!\omega_d\omega_{s+1}^2} \mathbb{E}V_{d-1}(P_{\ell,d}^\beta) \cdot Q^{\frac{s}{2}},$$

with $\mathbb{E}V_{d-1}(P_{\ell,d}^\beta)$ given as above.

Similar formulas can be derived for $\mathbb{E}\Phi_k^{0,s}(P_{\ell,d}^\beta)$, where $k \in \{0, \dots, d-1\}$, $s \in \mathbb{N}_0$ or $k = d$, $s = 0$, from results provided in [31] in combination with Lemma 5.1. The same is true for some other classes of isotropic random polytopes, including beta'-polytopes or symmetric versions of beta- and beta'-polytopes. For example for the expected intrinsic volumes of a beta-polytope Proposition 2.3 in [31] yields

$$\mathbb{E}V_k(P_{\ell,d}^\beta) = \binom{d}{k} \frac{\kappa_d}{\kappa_k \kappa_{d-k}} \mathbb{E}V_k(P_{\ell,k}^{\beta+\frac{d-k}{2}}).$$

5.2 Simulation study

In this section we simulate specific beta-polytopes in dimension 2 and 4 and determine the Minkowski tensors of the resulting polytopes from the implementation of our algorithm. Since the formulas from Section 5.1 simplify for $d = 2$ and $\beta \in \{-\frac{1}{2}, \frac{1}{2}\}$, we focus on these two values for β (also for $d = 4$). Table 7 shows the results for the expected volume and surface area of a 2- and a 4-dimensional beta-polytope with the choice $\ell = 10$. For $d = 2$ we also simulated the case $\ell = 100$ and obtained similar results. Furthermore, Table 8 contains the results for the expectation of the tensor $\Phi_1^{0,2}(P_{10,2}^\beta)_{i,j}$ (left) resp. $\Phi_1^{0,4}(P_{10,2}^\beta)_{i,j,k,l}$, and Table 9 gives the results for the expectation of the tensor $\Phi_3^{0,2}(P_{10,4}^\beta)_{i,j}$.

Table 7: Results for 2- and 4-dimensional beta-polytopes $P_{10,d}^\beta$. We intersected the simulated polytope with a grid of resolution 0.005 (resp. 0.02 for $d = 4$). The parameter choices were $n = 50$ and $R_n = 1$ (resp. $R_n = 0.5$ for $d = 4$). We took the average of 50 (resp. 10 for $d = 4$) renditions and computed the exact values with the formulas of Section 5.1. The table shows the values of the expectation $\mathbb{E} \left[V_k \left(P_{10,d}^\beta \right) \right]$.

d	k	β	Exact values	Algorithm	d	k	β	Exact values	Algorithm
2	1	$\frac{1}{2}$	2.08...	2.05(3)	4	3	$\frac{1}{2}$	0.81...	0.84(4)
2	1	$-\frac{1}{2}$	2.57...	2.57(3)	4	3	$-\frac{1}{2}$	1.35...	1.56(8)
2	2	$\frac{1}{2}$	1.06...	1.03(3)	4	4	$\frac{1}{2}$	0.107...	0.093(8)
2	2	$-\frac{1}{2}$	1.71...	1.72(6)	4	4	$-\frac{1}{2}$	0.21...	0.23(2)

Table 8: Results for 2-dimensional beta-polytopes $P_{10,2}^\beta$. We intersected the simulated polytope with a grid of resolution 0.005. The parameter choices were $n = 50$ and $R_n = 1$. We took the average of 50 (left) resp. 10 (right) renditions and computed the exact values with the formulas of Section 5.1. The table shows the values of

$\mathbb{E} \left[\Phi_1^{0,2}(P_{10,2}^\beta)_{i,j} \right]$					$\mathbb{E} \left[\Phi_1^{0,4}(P_{10,2}^\beta)_{l,l,l,l} \right]$			
β	i	j	Exact values	Algorithm	β	l	Exact values	Algorithm
$\frac{1}{2}$	1	1	0.083...	0.084(2)	$\frac{1}{2}$	1	0.0025...	0.0025(1)
$\frac{1}{2}$	1	2	0	-0.002(2)	$\frac{1}{2}$	2	0.0025...	0.0023(1)
$\frac{1}{2}$	2	2	0.083...	0.084(2)	$-\frac{1}{2}$	1	0.0031...	0.0030(1)
$-\frac{1}{2}$	1	1	0.102...	0.102(2)	$-\frac{1}{2}$	2	0.0031...	0.0031(1)
$-\frac{1}{2}$	1	2	0	0.001(2)				
$-\frac{1}{2}$	2	2	0.102...	0.101(2)				

The obtained values for index tuples (i, j, k, l) (for the tensor of rank 4), where not all entries are the same, were all not greater than $1.1 \cdot 10^{-3}$ (here the exact values are 0).

6 Experimental data

Finally, we apply our methods to real data, more specifically, to two distinct use cases. The first example is a collection of metallic grains that can be considered to be (or at least well approximated by) sets of positive reach. The second example are nanorough surfaces that exhibit deep cuts and high ridges, i.e., they are clearly no sets of positive reach, but they can be thought of as finite unions of compact sets with positive reach. By our Theorem 3.4, we can use our methods to estimate the interfacial tensor $\Phi_1^{0,2}$.

6.1 Metallic grains

We first apply our algorithm and code to a real data set published in [60] of a polycrystalline material, more specifically, of a nickel-based superalloy; see [60], for further details. The data set

Table 9: Results for 4-dimensional beta-polytopes $P_{10,4}^\beta$. We intersected the simulated polytopes with a grid of resolution 0.02. The parameter choices were $n = 50$ and $R_n = 0.5$. We took the average of 10 renditions and computed the exact values with the formulas of Section 5.1. The table shows the values of the expectation $\mathbb{E} \left[\Phi_3^{0,2}(P_{10,4}^\beta)_{i,j} \right]$.

β	i	j	Exact values	Algorithm	β	i	j	Exact values	Algorithm
$\frac{1}{2}$	1	1	0.016...	0.010(2)	$-\frac{1}{2}$	1	1	0.027...	0.022(3)
$\frac{1}{2}$	2	2	0.016...	0.011(1)	$-\frac{1}{2}$	2	2	0.027...	0.020(3)
$\frac{1}{2}$	3	3	0.016...	0.011(1)	$-\frac{1}{2}$	3	3	0.027...	0.022(4)
$\frac{1}{2}$	4	4	0.016...	0.014(2)	$-\frac{1}{2}$	4	4	0.027...	0.019(2)

The obtained values for $j \neq i$ were all not greater than $2.2 \cdot 10^{-3}$ (here the exact values are 0).

set contains, among others, 2546 individual grains, each represented by a set of voxel centers; see Figure 2, for three examples. The resolution of the grid is $1 \mu\text{m}$. To exclude numerical artifacts, we apply a data cut and only consider grains with at least 500 voxel centers, which results in a data set with 2180 grains. For each grain, we took the average over 10 renditions. We varied R_n between $4 \cdot R_1$ and $24 \cdot R_1$. The results from Figure 3 and 4 refer to the choice $R_n = 24 \cdot R_1$.

Figure 3 shows histograms of the estimated volumes and surface areas, respectively. The distributions peak at very small values, but they exhibit comparatively strong tails. Interestingly, the tails are more pronounced for the volumes than the surface areas. We also estimated the tensors $\Phi_k^{0,2}$, $k \in \{0, 1, 2, 3\}$. Figure 4 shows a histogram of the ratios between the smallest and biggest absolute eigenvalue for the tensors $\Phi_1^{0,2}$ and $\Phi_2^{0,2}$. These ratios represent scalar indices of anisotropy, which intuitively quantify the degree of anisotropy with respect to the corresponding Minkowski tensor, and which have already been successfully applied in physics [56, 57, 58, 34, 37]. For the metallic grains, these indices detect a higher degree of anisotropy with respect to the curvature than the surface area.

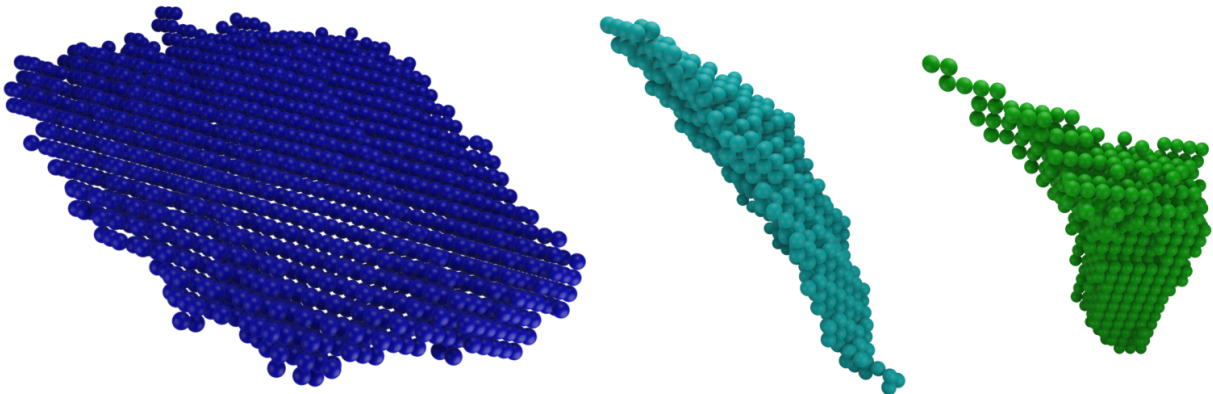


Figure 2: Examples of three distinct metallic grains that are represented by voxel centers. Here, each voxel center is indicated by a ball with a diameter equal to the lattice spacing, i.e., $1 \mu\text{m}$. The underlying experimental data of the grains is from [60].

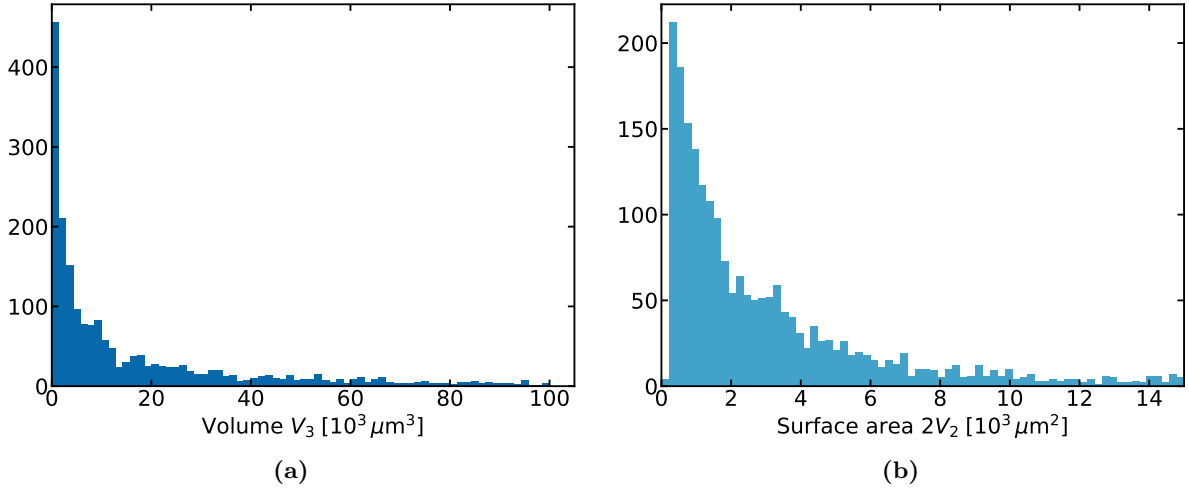


Figure 3: Non-normalized histograms of the estimated volumes (a) and surface areas (b) of the metallic grains from Section 6.1. Besides a large number of small cells, we observe a few exceptionally large cells. For better visualization, only a range of values is shown, i.e., the most extreme cases are excluded here. The underlying experimental data of the grains is from [60].

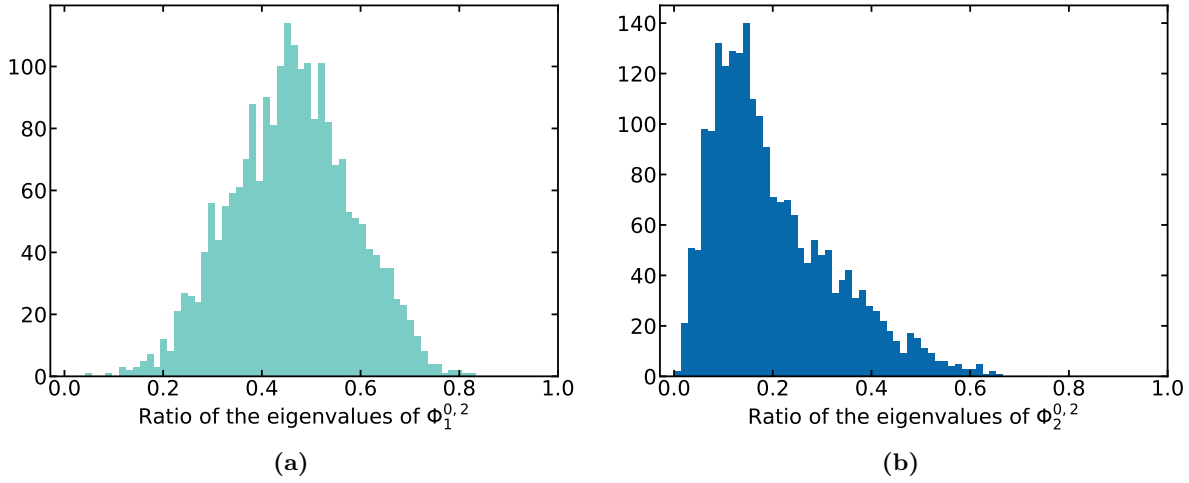


Figure 4: Non-normalized histograms of anisotropy indices for the metallic grains from Section 6.1. More specifically, the plots show histograms of the ratios between the smallest and largest absolute eigenvalues of the interfacial tensor $\Phi_1^{0,2}$ (a) and the curvature tensor $\Phi_2^{0,2}$ (b). The underlying experimental data of the grains is from [60].

6.2 Nanorough surfaces

Next, we apply our algorithm to a distinctly different experimental data set, a nanorough surface from [59], measured via atomic force microscopy (AFM). The roughness at the nano scale, i.e., an order of magnitude above atomic resolution, was obtained by a specific etching protocol; see [59] for further details. Both protocol and three-dimensional visualizations of the data sets (see Figure 5) suggest that the nanorough surface can be described (or at least approximated) by a finite union of compact sets with positive reach.

Table 10: Estimated values of the surface and the ratio of the eigenvalues of the tensor $\Phi_2^{0,2}$ in comparison with triangulation results based on data from [59]. For the surface estimation with the result of Theorem 4.5 we used Remark 4.6. We used several samples with the same RMS value. The underlying experimental data of the nanorough surfaces is from [59].

RMS [nm]	Triangulation		Least Squares		Theorem 4.5	
	Surface [μm^2]	Ratio EV	Surface [μm^2]	Ratio EV	Surface [μm^2]	Ratio EV
7	11.6	0.285	13.6	0.102	19.1	0.204
	11.6	0.287	13.5	0.110	19.1	0.204
	11.7	0.295	13.7	0.138	19.1	0.205
24	12.7	0.371	15.6	0.205	19.6	0.231
	12.4	0.359	15.0	0.205	19.5	0.227
	12.4	0.308	15.1	0.098	19.6	0.229
35	12.2	0.343	14.7	0.160	19.9	0.255
	12.5	0.360	15.2	0.184	20.0	0.259
	12.3	0.326	14.9	0.155	19.9	0.253
	12.4	0.354	15.0	0.178	19.9	0.255

We analyze ten samples in total with three different values of the root mean square (RMS) of height distribution (7 nm, 24 nm, and 35 nm). Each sample is measured within a scan window of size $3 \mu\text{m} \times 3 \mu\text{m}$ and a resolution of 512×512 pixels, i.e., each surface is represented by a grid of three-dimensional points, where the z -coordinate represents the height of the surface at the corresponding (x, y) position. We varied R_n between 12.5 and 250. The results from Table 10

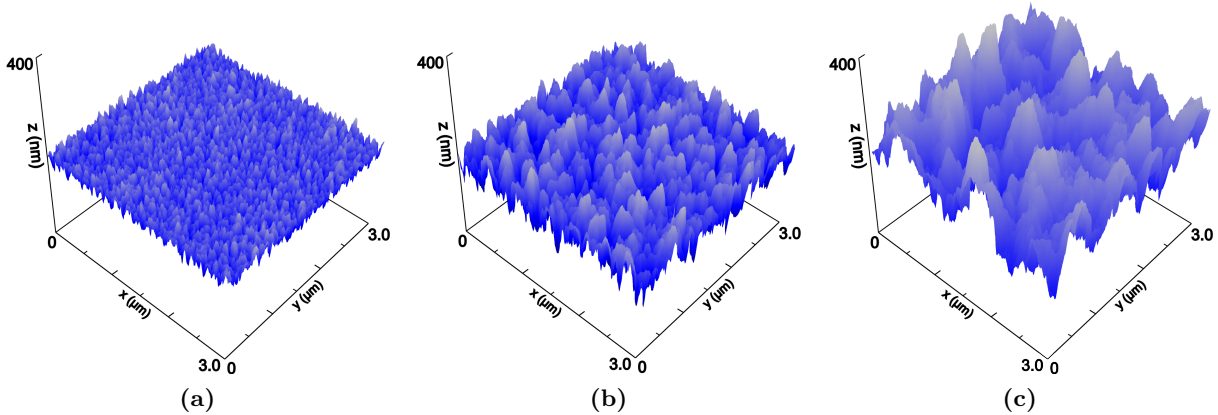


Figure 5: Examples of nanorough surfaces from Table 10 with three different degrees of roughness, i.e., an RMS value of (a) 7 nm, (b) 24 nm, and (c) 35 nm. The data is taken from [59]; the figures have been created by Jens Uwe Neurohr.

refer to the value $R_n = 25$, which is about 4 times the average nearest neighbor distance in the data. This rule of thumb balances robustness (due to a large range of radii) and accuracy (resolving fine details of the nanorough structure).

We compare our estimates with those from a triangulated data set as in [59] using methods from [58]. Considering how rough our samples are, and hence challenging for our method of extrapolation, we observe a relatively good agreement of our method with the results from the triangulated data. The Voronoi estimator tends to estimate slightly larger values of the surface area and higher degrees of anisotropy (i.e., smaller values of the anisotropy index). Importantly, the trend between samples agrees for both methods.

Acknowledgments

We thank Karin Jacobs and Christian Spengler for providing their data of nanorough surfaces, and Jens Uwe Neurohr for Figure 5. This work was supported in part by the Deutsche Forschungsgemeinschaft (DFG, German Research Foundation) through the SPP 2265, under grant numbers HU 1874/5-1, ME 1361/16-1, KL 3391/2-2, WI 5527/1-1, and LO 418/25-1, as well as by the Helmholtz Association and the DLR via the Helmholtz Young Investigator Group “DataMat”.

References

- [1] P. M. Adler, J.-F. Thovert, and V. V. Mourzenko. *Fractured Porous Media*. Oxford Univ. Press, Oxford, first edition, 2013. 2
- [2] R. J. Adler and J. E. Taylor. *Random Fields and Geometry*. Springer Monographs in Mathematics. Springer, New York, 2007. 2
- [3] R. T. Armstrong, J. E. McClure, V. Robins, Z. Liu, C. H. Arns, S. Schlüter, and S. Berg. Porous Media Characterization Using Minkowski Functionals: Theories, Applications and Future Directions. *Transp Porous Med*, 130:305–335, 2019. 2
- [4] C. H. Arns, M. A. Knackstedt, and K. Mecke. 3D structural analysis: Sensitivity of Minkowski functionals. *J. Microsc.*, 240:181, 2010. 2
- [5] C. H. Arns, M. A. Knackstedt, and K. R. Mecke. Reconstructing Complex Materials via Effective Grain Shapes. *Phys. Rev. Lett.*, 91:215506, 2003. 2
- [6] M. Barbosa, T. Maddess, S. Ahn, and T. Chan-Ling. Novel morphometric analysis of higher order structure of human radial peri-papillary capillaries: Relevance to retinal perfusion efficiency and age. *Sci Rep*, 9:1–16, 2019. 2
- [7] M. Barbosa, R. Natoli, K. Valter, J. Provis, and T. Maddess. Integral-geometry characterization of photobiomodulation effects on retinal vessel morphology. *Biomed. Opt. Express*, *BOE*, 5:2317–2332, 2014. 2
- [8] C. Beisbart, M. S. Barbosa, H. Wagner, and L. d. F. Costa. Extended morphometric analysis of neuronal cells with Minkowski valuations. *Eur. Phys. J. B*, 52:531–546, 2006. 2

- [9] Å. Björck. *Numerical methods for least squares problems*. Society for Industrial and Applied Mathematics (SIAM), Philadelphia, PA, second edition, 2024. 19
- [10] A. Böbel and C. Rätz. Kinetics of fluid demixing in complex plasmas: Domain growth analysis using Minkowski tensors. *Phys. Rev. E*, 94:013201, 2016. 2
- [11] S. J. P. Callens, D. C. Tourolle né Betts, R. Müller, and A. A. Zadpoor. The local and global geometry of trabecular bone. *Acta Biomaterialia*, 130:343–361, 2021. 2
- [12] S. N. Chiu, D. Stoyan, W. S. Kendall, and J. Mecke. *Stochastic Geometry and Its Applications*. Wiley, Chichester, third edition, 2013. 2
- [13] H. Cohn and N. Elkies. New upper bounds on sphere packings I. *Ann. Math.*, 157:689–714, 2003. 2
- [14] C. Collischon, M. A. Klatt, A. J. Banday, M. Sasaki, and C. Rätz. Morphometry on the sphere: Cartesian and irreducible Minkowski tensors explained and implemented. *Commun Phys*, 7:1–10, 2024. 2
- [15] C. Collischon, M. Sasaki, K. Mecke, S. D. Points, and M. A. Klatt. Tracking down the origin of superbubbles and supergiant shells in the Magellanic Clouds with Minkowski tensor analysis. *A&A*, 653:A16, 2021. 2
- [16] B. Ebner, N. Henze, M. A. Klatt, and K. Mecke. Goodness-of-fit tests for complete spatial randomness based on Minkowski functionals of binary images. *Electron J. Stat.*, 12:2873–2904, 2018. 2
- [17] F. Ernesti, M. Schneider, S. Winter, D. Hug, G. Last, and T. Böhlke. Characterizing digital microstructures by the Minkowski-based quadratic normal tensor. *Mathematical Methods in the Applied Sciences*, 46(1):961–985, 2023. 2
- [18] J. R. Gott III, C. Park, R. Juskiewicz, W. E. Bies, D. P. Bennett, F. R. Bouchet, and A. Stebbins. Topology of microwave background fluctuations - Theory. *ApJ*, 352:1, 1990. 2
- [19] J.-P. Hansen and I. R. McDonald. *Theory of Simple Liquids: With Applications to Soft Matter*. Academic Press, Amsterdam, 4th edition, 2013. 2
- [20] P. C. Hansen, V. Pereyra, and G. Scherer. *Least squares data fitting with applications*. Johns Hopkins University Press, Baltimore, MD, 2013. 19
- [21] D. Hug, M. Kiderlen, and A. M. Svane. Voronoi-Based Estimation of Minkowski Tensors from Finite Point Samples. *Discrete Comput. Geom.*, 57:545–570, 2017. 3, 10, 12, 18, 19
- [22] D. Hug, G. Last, and M. Schulte. Second-order properties and central limit theorems for geometric functionals of Boolean models. *Ann. Appl. Probab.*, 26(1):73–135, 2016. 16
- [23] D. Hug, G. Last, and W. Weil. A local Steiner-type formula for general closed sets and applications. *Math. Z.* 246, pages 237–272, 2004. 6, 7, 8, 9, 11
- [24] D. Hug and M. Santilli. Curvature measures and soap bubbles beyond convexity. *Advances in Mathematics*, 411, 2022. 6, 7

- [25] D. Hug and R. Schneider. Tensor valuations and their local versions. In *Tensor valuations and their applications in stochastic geometry and imaging*, volume 2177 of *Lecture Notes in Mathematics*, pages 27–65. Springer, 2017. [4](#), [6](#)
- [26] D. Hug and W. Weil. *Lectures on Convex Geometry*, volume 286 of *Graduate Texts in Mathematics*. Springer, Cham, 2020. [4](#)
- [27] D. Hug and J. Weis. Kinematic formulae for tensorial curvature measures. *Annali di Matematica Pura ed Applicata (1923 -)*, 197:1349–1384, 2018. [24](#), [26](#)
- [28] E. B. V. Jensen and M. Kiderlen, editors. *Tensor valuations and their applications in stochastic geometry and imaging*, volume 2177 of *Lecture Notes in Mathematics*. Springer, Cham, 2017. [2](#)
- [29] H. Jiang and C. H. Arns. Fast Fourier transform and support-shift techniques for pore-scale microstructure classification using additive morphological measures. *Phys. Rev. E*, 101:033302, 2020. [2](#)
- [30] P. Joby, P. Chingambam, T. Ghosh, V. Ganesan, and C. Ravikumar. Search for anomalous alignments of structures in Planck data using Minkowski Tensors. *J. Cosmol. Astropart. Phys.*, 2019:009–009, 2019. [2](#)
- [31] Z. Kabluchko, D. Temesvari, and C. Thäle. Expected intrinsic volumes and facet numbers of random beta-polytopes. *Mathematische Nachrichten*, 292:79–105, 2019. [26](#), [27](#)
- [32] Z. Kabluchko, C. Thäle, and D. Zaporozhets. Beta polytopes and Poisson polyhedra: f-vectors and angles. *Advances in Mathematics*, 374:107333, 2020. [25](#), [26](#)
- [33] M. A. Klatt, M. Hörmann, and K. Mecke. Characterization of anisotropic Gaussian random fields by Minkowski tensors. *J. Stat. Mech.*, 2022:043301, 2022. [2](#)
- [34] M. A. Klatt, G. Last, K. Mecke, C. Redenbach, F. M. Schaller, and G. E. Schröder-Turk. Cell Shape Analysis of Random Tessellations Based on Minkowski Tensors. In E. B. Vedel Jensen and M. Kiderlen, editors, *Tensor Valuations and Their Applications in Stochastic Geometry and Imaging*, volume 2177 of *Lecture Notes in Mathematics*, pages 385–421. Springer International Publishing, Cham, 2017. [2](#), [29](#)
- [35] M. A. Klatt and K. Mecke. Detecting structured sources in noisy images via Minkowski maps. *EPL*, 128:60001, 2020. [2](#)
- [36] M. A. Klatt, G. E. Schröder-Turk, and K. Mecke. Anisotropy in finite continuum percolation: Threshold estimation by Minkowski functionals. *J. Stat. Mech. Theor. Exp.*, 2017:023302, 2017. [2](#)
- [37] M. A. Klatt, G. E. Schröder-Turk, and K. Mecke. Mean-intercept anisotropy analysis of porous media. II. Conceptual shortcomings of the MIL tensor definition and Minkowski tensors as an alternative. *Med. Phys.*, 44:3663–3675, 2017. [2](#), [29](#)
- [38] D. Legland, K. Kiêu, and M.-F. Devaux. Computation of Minkowski measures on 2d and 3d binary images. *Image Anal Stereol*, 26:83, 2011. [3](#)

- [39] H. Mantz, K. Jacobs, and K. Mecke. Utilising Minkowski Functionals for Image Analysis. *J. Stat. Mech.*, 12:P12015, 2008. [3](#)
- [40] K. Mecke. Integral Geometry and Statistical Physics. *Int. J. Mod. Phys. B*, 12:861–899, 1998. [2](#)
- [41] K. R. Mecke, Th. Buchert, and H. Wagner. Robust morphological measures for large-scale structure in the universe. *Astron. Astrophys.*, 288:697, 1994. [2](#)
- [42] K. R. Mecke and D. Stoyan, editors. *Statistical Physics and Spatial Statistics: The Art of Analyzing and Modeling Spatial Structures and Pattern Formation*. Lecture Notes in Physics. Springer, Berlin ; New York, 2000. [2](#)
- [43] Q. Mérigot, M. Ovsjanikov, and L. J. Guibas. Voronoi-based curvature and feature estimation from point clouds. *IEEE Transactions on Visualization and Computer Graphics*, 17(6):743–756, 2011. [3](#)
- [44] J. Ohser and F. Mücklich. *Statistical Analysis of Microstructures in Materials Science*. Statistics in Practice. John Wiley, Chichester [England]; New York, 2000. [2](#)
- [45] J. Ohser and K. Schladitz. *3D Images of Materials Structures: Processing and Analysis*. Wiley-VCH, Weinheim, 2009. [2](#)
- [46] A. Okabe, B. Boots, K. Sugihara, and S. N. Chiu. *Spatial Tessellations: Concepts and Applications of Voronoi Diagrams*. Wiley Series in Probability and Statistics. Wiley, Chichester ; New York, 2nd ed edition, 2000. [2](#)
- [47] D. Pabst. Voromink. <https://zenodo.org/records/14614277>, 2025. DOI: 10.5281/zenodo.14614277. [10](#), [21](#)
- [48] J. Rataj. On boundaries of unions of sets with positive reach. *Beiträge Algebra Geom.*, 46(2):397–404, 2005. [8](#)
- [49] J. Rataj and M. Zähle. *Curvature measures of singular sets*. Springer Monographs in Mathematics. Springer, Cham, 2019. [6](#), [7](#)
- [50] C. Râth, R. Monetti, J. Bauer, I. Sidorenko, D. Müller, M. Matsuura, E.-M. Lochmüller, P. Zysset, and F. Eckstein. Strength through structure: Visualization and local assessment of the trabecular bone structure. *New J. Phys.*, 10:125010, 2008. [2](#)
- [51] M. C. Röttger, A. Sanner, L. A. Thimons, T. Junge, A. Gujrati, J. M. Monti, W. G. Nöhring, T. D. B. Jacobs, and L. Pastewka. Contact.engineering—Create, analyze and publish digital surface twins from topography measurements across many scales. *Surf. Topogr.: Metrol. Prop.*, 10:035032, 2022. [2](#)
- [52] J. Schmalzing and K. M. Górski. Minkowski functionals used in the morphological analysis of cosmic microwave background anisotropy maps. *Monthly Notices of the Royal Astronomical Society*, 297:355–365, 1998. [2](#)
- [53] R. Schneider. *Convex Bodies: The Brunn–Minkowski Theory*. Cambridge University Press, second expanded edition, 2014. [5](#)

- [54] R. Schneider. Valuations on convex bodies: the classical basic facts. In *Tensor valuations and their applications in stochastic geometry and imaging*, volume 2177 of *Lecture Notes in Mathematics*, pages 1–25. Springer, 2017. [4](#)
- [55] R. Schneider and W. Weil. *Stochastic and Integral Geometry (Probability and Its Applications)*. Springer, Berlin, 2008. [2](#)
- [56] G. Schröder-Turk, S. Kapfer, B. Breidenbach, C. Beisbart, and K. Mecke. Tensorial Minkowski functionals and anisotropy measures for planar patterns. *J. Micr.*, 238:57–74, 2010. [2](#), [29](#)
- [57] G. E. Schröder-Turk, W. Mickel, S. C. Kapfer, M. A. Klatt, F. M. Schaller, M. J. F. Hoffmann, N. Kleppmann, P. Armstrong, A. Inayat, D. Hug, M. Reichelsdorfer, W. Peukert, W. Schwieger, and K. Mecke. Minkowski Tensor Shape Analysis of Cellular, Granular and Porous Structures. *Adv. Mater.*, 23:2535–2553, 2011. [2](#), [29](#)
- [58] G. E. Schröder-Turk, W. Mickel, S. C. Kapfer, F. M. Schaller, B. Breidenbach, D. Hug, and K. Mecke. Minkowski tensors of anisotropic spatial structure. *New J. Phys.*, 15:083028, 2013. [29](#), [32](#)
- [59] C. Spengler, F. Nolle, J. Mischo, T. Faidt, S. Grandthyll, N. Thewes, M. Koch, F. Müller, M. Bischoff, M. A. Klatt, and K. Jacobs. Strength of bacterial adhesion on nanostructured surfaces quantified by substrate morphometry. *Nanoscale*, 11:19713–19722, 2019. [2](#), [3](#), [30](#), [31](#), [32](#)
- [60] J. C. Stinville, J. M. Hestroffer, M. A. Charpagne, A. T. Polonsky, M. P. Echlin, C. J. Torbet, V. Valle, K. E. Nygren, M. P. Miller, O. Klaas, A. Loghin, I. J. Beyerlein, and T. M. Pollock. Multi-modal Dataset of a Polycrystalline Metallic Material: 3D Microstructure and Deformation Fields. *Sci Data*, 9:460, 2022. [2](#), [3](#), [28](#), [29](#), [30](#)
- [61] A. M. Svane. Estimation of Intrinsic Volumes from Digital Grey-Scale Images. *J Math Imaging Vis*, 49:352–376, 2014. [3](#)
- [62] A. M. Svane. Estimation of Minkowski tensors from digital grey-scale images. *Image Anal. Stereol.*, 33:51, 2014. [3](#)
- [63] A. M. Svane. Valuations in Image Analysis. In E. B. V. Jensen and M. Kiderlen, editors, *Tensor Valuations and Their Applications in Stochastic Geometry and Imaging*, volume 2177, pages 435–454. Springer International Publishing, Cham, 2017. [3](#)
- [64] S. Torquato. *Random Heterogeneous Materials*, volume 16 of *Interdisciplinary Applied Mathematics*. Springer, New York, second edition, 2002. [2](#)
- [65] E. Vanmarcke. *Random Fields: Analysis and Synthesis*. World Scientific, 2010. [2](#)
- [66] J. F. Ziegel, J. R. Nyengaard, and E. B. Vedel Jensen. Estimating Particle Shape and Orientation Using Volume Tensors. *Scand. J. Stat.*, 42:813–831, 2015. [2](#)
- [67] C. Zong. *Sphere Packings*. Universitext. Springer, New York, 1999. [2](#)

A Further simulation results

In this section, we provide additional simulation results for the algorithm described in the paper, based on solving a least-squares problem. The following tables can be found on the subsequent pages:

- Table 11: Simulation results for the 2-dimensional rectangle $[-\frac{3}{2}, \frac{3}{2}] \times [-\frac{5}{2}, \frac{5}{2}]$
- Table 12: Simulation results for a 2-dimensional rectangle with rounded vertices. Specifically, we mean the parallel set of a rectangle. The parallel set of a compact set K with parameter r_0 is the set of all points with a distance less than r_0 to K .
- Table 13: Simulation results for the 3-dimensional rectangle $[-\frac{1}{2}, \frac{1}{2}] \times [-1, 1] \times [-\frac{3}{2}, \frac{3}{2}]$.

Table 11: Results for the 2-dimensional rectangle $[-\frac{3}{2}, \frac{3}{2}] \times [-\frac{5}{2}, \frac{5}{2}]$ intersected with a grid of resolution $a = 0.01$. The parameter choices were $n = 50$ and $R_n = 2$. We took the average of 50 renditions. All values are rounded to the fourth significant digit.

Tensors	Values	Algorithm	Tensors	Values	Algorithm
$\Phi_0^{0,0}$	1	0.9999	$\Phi_1^{0,0}$	8	8.000
$\Phi_2^{0,0}$	15	15.00	$(\Phi_0^{1,0})_1$	0	$-4.249 \cdot 10^{-5}$
$(\Phi_0^{1,0})_2$	0	$5.899 \cdot 10^{-6}$	$(\Phi_1^{1,0})_1$	0	$1.232 \cdot 10^{-4}$
$(\Phi_1^{1,0})_2$	0	$1.137 \cdot 10^{-4}$	$(\Phi_2^{1,0})_1$	0	$-6.011 \cdot 10^{-5}$
$(\Phi_2^{1,0})_2$	0	$-2.237 \cdot 10^{-4}$	$(\Phi_0^{0,1})_1$	0	$-2.822 \cdot 10^{-5}$
$(\Phi_0^{0,1})_2$	0	$-2.609 \cdot 10^{-5}$	$(\Phi_1^{0,1})_1$	0	$1.988 \cdot 10^{-4}$
$(\Phi_1^{0,1})_2$	0	$1.109 \cdot 10^{-4}$	$(\Phi_2^{0,1})_1$	0	$-3.995 \cdot 10^{-4}$
$(\Phi_2^{0,1})_2$	0	$3.05 \cdot 10^{-5}$	$(\Phi_0^{0,2})_{1,1}$	0.07958	0.07958
$(\Phi_0^{0,2})_{1,2}$	0	$4.382 \cdot 10^{-6}$	$(\Phi_0^{0,2})_{2,2}$	0.07958	0.07957
$(\Phi_1^{0,2})_{1,1}$	0.3979	0.3979	$(\Phi_1^{0,2})_{1,2}$	0	$-1.301 \cdot 10^{-5}$
$(\Phi_1^{0,2})_{2,2}$	0.2387	0.2387	$(\Phi_2^{0,2})_{1,1}$	0	$5.863 \cdot 10^{-5}$
$(\Phi_2^{0,2})_{1,2}$	0	$9.168 \cdot 10^{-6}$	$(\Phi_2^{0,2})_{2,2}$	0	$5.234 \cdot 10^{-5}$
$(\Phi_0^{2,0})_{1,1}$	1.125	1.125	$(\Phi_0^{2,0})_{1,2}$	0	$-6.546 \cdot 10^{-7}$
$(\Phi_0^{2,0})_{2,2}$	3.125	3.125	$(\Phi_1^{2,0})_{1,1}$	6.75	6.750
$(\Phi_1^{2,0})_{1,2}$	0	$1.239 \cdot 10^{-5}$	$(\Phi_1^{2,0})_{2,2}$	14.58	14.58
$(\Phi_2^{2,0})_{1,1}$	5.625	5.625	$(\Phi_2^{2,0})_{1,2}$	0	$-1.561 \cdot 10^{-5}$
$(\Phi_2^{2,0})_{2,2}$	15.63	15.62	$(\Phi_0^{1,1})_{1,1}$	0.4775	0.4774
$(\Phi_0^{1,1})_{1,2}$	0	$-7.008 \cdot 10^{-6}$	$(\Phi_0^{1,1})_{2,2}$	0.7958	0.7957
$(\Phi_1^{1,1})_{1,1}$	2.387	2.388	$(\Phi_1^{1,1})_{1,2}$	0	$1.739 \cdot 10^{-5}$
$(\Phi_1^{1,1})_{2,2}$	2.387	2.388	$(\Phi_2^{1,1})_{1,1}$	0	$-6.019 \cdot 10^{-4}$
$(\Phi_2^{1,1})_{1,2}$	0	$-3.425 \cdot 10^{-6}$	$(\Phi_2^{1,1})_{2,2}$	0	$-5.301 \cdot 10^{-4}$

The standard errors of the values were all not greater than $9.5 \cdot 10^{-4}$. The 0 entries are rounded. Their absolute values were all not greater than $6.1 \cdot 10^{-4}$.

Table 12: Results for a 2-dimensional rectangle with rounded vertices intersected with a grid of resolution $a = 0.005$. Here R_{r_0} denotes the parallel set of the rectangle $[-\frac{3}{2}, \frac{3}{2}] \times [-\frac{5}{2}, \frac{5}{2}]$ with parameter $r_0 > 0$. The parameter choices were $n = 5$ and $R_n = 1$. We took the average of 10 renditions.

Tensors	Values	Algorithm	Tensors	Values	Algorithm
$\Phi_0^{0,0} (R_{\frac{1}{4}})$	0.999	1	$\Phi_1^{0,0} (R_{\frac{1}{4}})$	8.784	8.785
$\Phi_2^{0,0} (R_{\frac{1}{4}})$	19.194	19.196	$\Phi_1^{0,2} (R_{\frac{1}{4}})$	$\begin{pmatrix} 0.269 & 0 \\ 0 & 0.429 \end{pmatrix}$	$\begin{pmatrix} 0.270 & 0 \\ 0 & 0.429 \end{pmatrix}$
$\Phi_0^{0,0} (R_{\frac{1}{2}})$	0.999	1	$\Phi_1^{0,0} (R_{\frac{1}{2}})$	9.571	9.571
$\Phi_2^{0,0} (R_{\frac{1}{2}})$	23.782	23.785	$\Phi_1^{0,2} (R_{\frac{1}{2}})$	$\begin{pmatrix} 0.301 & 0 \\ 0 & 0.460 \end{pmatrix}$	$\begin{pmatrix} 0.301 & 0 \\ 0 & 0.460 \end{pmatrix}$
$\Phi_0^{0,0} (R_1)$	0.999	1	$\Phi_1^{0,0} (R_1)$	11.143	11.142
$\Phi_2^{0,0} (R_1)$	34.134	34.142	$\Phi_1^{0,2} (R_1)$	$\begin{pmatrix} 0.363 & 0 \\ 0 & 0.522 \end{pmatrix}$	$\begin{pmatrix} 0.364 & 0 \\ 0 & 0.523 \end{pmatrix}$

Table 13: Results for the 3-dimensional rectangle $[-\frac{1}{2}, \frac{1}{2}] \times [-1, 1] \times [-\frac{3}{2}, \frac{3}{2}]$ intersected with a grid of resolution $a = 0.01$. The parameter choices were $n = 5$ and $R_n = 1$. We took the average of 28 renditions.

Tensors	Values	Algorithm	Tensors	Values	Algorithm
$\Phi_0^{0,0}$	1	1.005	$\Phi_1^{0,0}$	6	5.986
$\Phi_2^{0,0}$	11	11.051	$(\Phi_0^{0,2})_{1,1}$	0.080	0.075
$(\Phi_0^{0,2})_{2,2}$	0.080	0.079	$(\Phi_0^{0,2})_{3,3}$	0.080	0.078
$(\Phi_1^{0,2})_{1,1}$	0.398	0.406	$(\Phi_1^{0,2})_{2,2}$	0.318	0.319
$(\Phi_1^{0,2})_{3,3}$	0.239	0.243	$(\Phi_2^{0,2})_{1,1}$	0.478	0.472
$(\Phi_2^{0,2})_{2,2}$	0.239	0.238	$(\Phi_2^{0,2})_{3,3}$	0.159	0.156
$(\Phi_0^{2,0})_{1,1}$	0.125	0.126	$(\Phi_0^{2,0})_{2,2}$	0.5	0.500
$(\Phi_0^{2,0})_{3,3}$	1.125	1.126	$(\Phi_1^{2,0})_{1,1}$	0.667	0.665
$(\Phi_1^{2,0})_{2,2}$	2.333	2.333	$(\Phi_1^{2,0})_{3,3}$	4.5	4.497
$(\Phi_2^{2,0})_{1,1}$	0.958	0.960	$(\Phi_2^{2,0})_{2,2}$	2.833	2.835
$(\Phi_2^{2,0})_{3,3}$	5.625	5.629	$(\Phi_3^{2,0})_{1,1}$	0.25	0.249
$(\Phi_3^{2,0})_{2,2}$	1	0.999	$(\Phi_3^{2,0})_{3,3}$	2.25	2.248
$(\Phi_0^{1,1})_{1,1}$	0.159	0.159	$(\Phi_0^{1,1})_{2,2}$	0.318	0.319
$(\Phi_0^{1,1})_{3,3}$	0.478	0.475	$(\Phi_1^{1,1})_{1,1}$	0.796	0.795
$(\Phi_1^{1,1})_{2,2}$	1.273	1.272	$(\Phi_1^{1,1})_{3,3}$	1.432	1.437
$(\Phi_2^{1,1})_{1,1}$	0.955	0.958	$(\Phi_2^{1,1})_{2,2}$	0.955	0.956
$(\Phi_2^{1,1})_{3,3}$	0.955	0.952			